Nano Energy 127 (2024) 109781

Contents lists available at ScienceDirect

Nano Energy

journal homepage: www.elsevier.com/locate/nanoen

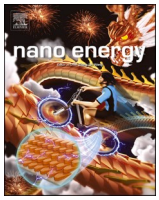

Full paper

Sustainable graphene production for solution-processed microsupercapacitors and multipurpose flexible electronics

Siva Sankar Nemala [a], João Fernandes [a], João Rodrigues [a,b], Vicente Lopes [a,c], Rui M.R. Pinto [a], K.B. Vinayakumar [a], Ernesto Placidi [d], Giovanni De Bellis [e,f], Pedro Alpuim [a,c], Rui S. Sampaio [g], Maria F. Montemor [g], Andrea Capasso [a,*]

[a] International Iberian Nanotechnology Laboratory, Braga 4715-330, Portugal
[b] Graphenest, Lugar da Estação, Edifício Vouga Park, Paradela do Vouga 3740-070, Portugal
[c] Center of Physics of the Universities of Minho and Porto, University of Minho, Braga 4710-057, Portugal
[d] Physics Department, Sapienza University of Rome, Rome 00185, Italy
[e] Research Center on Nanotechnology Applied to Engineering of Sapienza (CNIS), Sapienza University of Rome, Rome 00185, Italy
[f] Department of Astronautical, Electrical and Energy Engineering, Rome 00184, Italy
[g] Centro de Química Estrutural, CQE, Institute of Molecular Sciences, Departamento de Engenharia Química, Instituto Superior Técnico, Universidade de Lisboa, Lisboa 1049-001, Portugal

ARTICLE INFO

Keywords:
Liquid-phase processing
Green functional inks
Eco-friendly processes
Energy storage
EMI shielding
Wearable sensors

ABSTRACT

The growing demand for portable and wearable electronics, Internet of Things microdevices, and wireless sensor networks has led to the development of miniaturized energy storage devices, such as microsupercapacitors (mSCs). With excellent electrical conductivity and high surface area in a layered structure, graphene materials are ideal for mSCs, but current manufacturing methods still hinder their widespread integration. Here, we propose a sustainable approach for the rapid and eco-friendly production of few-layer graphene flakes based on the exfoliation of graphite in water by a combination of high-shear mixing and a high-pressure airless spray. An all-carbon composite paste with high electrical conductivity and tunable viscosity was designed to fabricate planar, interdigitated mSCs on polyethylene terephthalate (PET). The flexible, metal-free mSCs achieved a Coulombic efficiency close to 100%, with areal and volumetric capacitances of 6.16 mF cm^{-2} and 2.46 F cm^{-3}, respectively. The maximum energy density exceeds 200 μWh cm^{-3} with 91.5% capacitance retention after 10000 galvanostatic charge—discharge cycles. The mSCs retain the same performance when subjected to a wide bending range and can be easily modularized to adjust the voltage and capacitance outputs. Finally, high-performance coatings for electromagnetic interference shielding and wearable strain sensors are also fabricated to demonstrate the multipurpose applicability of the graphene-based paste.

1. Introduction

Graphene-based nanomaterials have been the subject of extensive academic and industrial research [1], motivated by graphene's properties (e.g., chemical stability, high surface area, high strength, flexibility, biocompatibility, superior thermal and electrical conductivity) [2–6]. This has spurred the realization of several technologies, including flexible electronics [7,8], sensors [9], supercapacitors [10–12], displays [13], biomedical systems [14] and next-generation solar cells [15–17]. Significant efforts aim to produce graphene materials with high yields and large, scalable volumes [18]. Liquid-phase exfoliation (LPE) allows the production of mono- or few-layer graphene (FLG) dispersions at a reasonable cost [19] by using a vast array of techniques: ultrasonication, high-shear (HS) mixing [20], wet-ball milling [21], microfluidization [22], homogenization [23], and wet-jet milling [24]. Taken individually, techniques such as ultrasonication and shear mixing remain unattractive for scaling up toward industrial production since they both have low yields and require long processing times and multiple cycles (up to 30 h and 60 h, respectively, to produce 1 g of exfoliated graphene flakes) [25,26]. The selection of suitable solvents is also crucial for efficiently exfoliating bulk graphite and stabilizing graphene dispersions against reagglomeration and sedimentation over time [27–29]. On the one

* Corresponding author.
E-mail address: andrea.capasso@inl.int (A. Capasso).

https://doi.org/10.1016/j.nanoen.2024.109781
Received 1 February 2024; Received in revised form 14 May 2024; Accepted 20 May 2024
Available online 21 May 2024

hand, N-methyl-2-pyrrolidone (NMP) [30] and N,N-dimethylformamide (DMF) [31] ($\gamma \approx 40 mJ \bullet m^{-2}$) have long been regarded as top-choice solvents owing to their favorable Hansen solubility parameters and ability to match the surface tension of graphene [32]. However, their acute human and environmental toxicity, combined with their high boiling points, not only limits the use of plastic substrates (requiring low treatment temperatures) but also hampers the agglomeration-free separation of exfoliated graphene sheets [15–17]. On the other hand, solvents such as water and ethanol, while tackling the latter issues thanks to their low boiling points, can lead to lower yields and potential reagglomeration [32]. In this case, surfactants (e.g., sodium cholate) can be added to achieve stable dispersion but at the cost of further post-processing for elimination [15,33]. Environmentally friendly graphene inks can be generated with solvents such as water and ethanol [34] or Cyrene™ [35–38], offering a viable alternative for the sustainable preparation of highly concentrated graphene dispersions. In most cases, LPE-produced graphene needs to be further processed and mixed in composites to comply with the requirements (in terms of concentration, viscosity, etc.) of the specific application and the different deposition techniques [29]. The selection of binders, additives, and/or other solvents is crucial for tuning and optimizing composite formulations. Binders (*e.g.,* acrylics, alkyls, cellulose, and rubber resins) are usually responsible for the interaction among filler particles (in this case, graphene flakes) and their adhesion to the substrate [27]. Among the additives, surfactants can improve wetting properties during deposition, while defoamers can reduce the surface tension of water-based inks to avoid bubble formation during mixing and deposition processes [39,40].

Nanoscale electroactive composites, such as supercapacitors, which have emerged as efficient materials due to their fast charge—discharge rates, long life, and simple structure, are in high demand for use in energy-storage devices [41]. Supercapacitors rely on fast and reversible adsorption/desorption of ions to store charges at electrode/electrolyte interfaces, thus attaining a very high power density (>10 000 W kg^{-1}) [42–48]. As such, they find applications in electronics [49], regenerative braking systems for electric vehicles [50] and biomedical devices [51], among others. Microsupercapacitors (mSCs) [52,53] are smaller and lighter devices [54,55] that are particularly suited for portable and wearable electronics [56–58] and can attain even higher power densities [52]. As key components, electrode materials should offer large electrochemically active surfaces and hierarchical porosity for ion diffusion and accumulation. Porous carbons, such as activated carbon, have been widely tested due to their low weight, high conductivity, and specific surface area [10]. However, they can entail high production costs, corrosion of equipment, and production-caused emission of toxic gases [59]. Graphene materials have been integrated into supercapacitor electrodes, contributing to high device performance (mostly by improving the electrochemical response, ensuring stability at high temperatures, and resisting the fading of performance typical of standard materials, such as metallic compounds) [60,61]. Concentrated graphene inks in NMP [12] and DMF [62] were printed to realize mSCs with high areal capacitance, and advancements in the LPE process contributed to upscaling the production of graphene-based mSCs [24,63,64]. To improve the electrochemical performance of these preliminary devices, different graphene-based composites have been proposed as advanced electrode materials [43,65,66]. Graphene sheets are prone to restack because of random aggregation during electrode fabrication, thus reducing the availability of ion-transport channels. Other carbon-based materials, such as carbon nanotubes (CNTs), have since been mixed with graphene sheets to serve as spacers and avoid the restacking issue while also promoting electrical percolation. Reduced graphene oxide/CNT composites were proposed as highly packed self-standing binder-free films suitable as electrodes for aqueous supercapacitors [66]. Nonetheless, CNTs are still expensive and difficult to produce in large quantities. In comparison, carbon black can be produced in large quantities and can offer high electrochemical performance as for mSC electrode material [67]. Highly conductive composites are required for several other applications, including electromagnetic interference (EMI) shielding and strain sensing. EMI shielding coatings act as barriers to screening devices from unwanted signals or electromagnetic noise generated by nearby electronics and limit distortion, crosstalk, or interference [68]. In addition to exhibiting high electrical conductivity, strong absorption, and minimal reflection of incoming electromagnetic waves [69], an ideal coating should be homogenous and uniform in thickness, with strong adhesion to the substrate. Metallic coatings usually exhibit excellent shielding performance, but they may generate secondary EM pollution via reflection. Moreover, metals are expensive, heavy and susceptible to corrosion, and their manufacturing requires high energy consumption and results in a large carbon footprint [70]. Conductive polymers are a potential low-cost alternative, but their conductivity is rather unsatisfactory, and their stability in harsh environments is limited [71]. Monolayer graphene is an ideal EMI shielding coating with the obvious limitation of a one-atom thickness [72]. Graphene-based materials and composites can be deposited in thicker coatings and attain high shielding effectiveness [73]. Wearable sensors are a class of lightweight and flexible devices that can be utilized for physical activity and health monitoring, among the many applications [74–77]. Textile sensors in particular have been designed in a variety of configurations [78–81] and are particularly suited for human motion detection [81]. In a textile strain sensor, the main challenge is the integration of conductive elements within the textile fibers, where the conductive elements should retain structural integrity and vary the electrical resistance gradually with strain and tension. Graphene materials and composites have shown promising results for developing textile-integrated wearable strain sensing elements, namely, for human motion detection and blood pulse measurements [82–84]. Several textile-integrated graphene-based strain gauges have shown variable gauge factors depending on the production and transfer methods used [85].

In this work, we propose a versatile and sustainable nanocarbon-based composite paste by a sustainable, scalable and inexpensive strategy. Few-layer graphene flake dispersions are prepared in water by combining HS mixing and HP atomization. The combination of these two techniques reduces the processing time while maximizing the produced volume (1 L/h, with a final concentration of 1.4 mg/mL) and is environmentally friendly. The dispersions remain stable, without sedimentation, for more than 6 months. The graphene flakes are mixed in a composite using only sustainable components, such as carbon black, gum Arabic (a natural binder), and Cyrene. By adjusting the graphene loading and rheological properties, we obtained a highly conductive paste that can be deposited by simple solution processing techniques, such as bar coating and screen printing. The paste was used in the fabrication of flexible mSC electrodes. To demonstrate the wide range of applicability of the paste, further proof-of-concept EMI shielding coatings and strain sensors were fabricated and tested.

2. Experimental

2.1. Materials

High-quality natural graphite (332461) (600–900 μm flake size), sodium deoxycholate (302954), dihydrolevoglucosenone (Cyrene, purity ≥ 98.5%, 807796) and gum arabic (9000015) were obtained from Sigma—Aldrich. The dispersing additive DISPERBYK-2012, the antifoaming agent BYK-022 and the percolation enhancer BYK-ES80 were supplied by BYK (a member of ALTANA). Carbon black (VXC Max 22) was obtained from CABOT. All the materials were used for the experiments without any further purification.

2.2. Preparation of FLG flake dispersions

Large-scale graphene production was achieved via LPE in water. This process combines two LPE methods: HS mixing and HP airless sprayer

exfoliation. Natural graphite powder at a 40 mg/mL concentration was added to 1250 mL of DI water supplemented with 1 mg/mL of SDC and 0.5 v% of DISPERBYK-2012 and BYK-022. The prepared mixture was stirred for 30 min to promote proper intercalation and wetting, thus obtaining a homogeneous dispersion. Then, the dispersion was further sheared with an HS mixer (Silverson L5M, standard mixing with an axial flow head) at 6000 rpm for 2 h using an ice bath to dissipate excess heat generated during mixing. This step allows natural graphite to experience fragmentation (from an initial average lateral size of 600–800 μm to 100–200 μm) and mild exfoliation (due to the short exfoliation time). This process was repeated four times to reach a total volume of 5 L, which was necessary for the following steps. Then, the resultant mixture was subjected to exfoliation through an airless sprayer (Magnum by Graco, truly airless A20 plus). In brief, following the shear mixing step, the mixture was sprayed into a container through an airless sprayer gun with a nozzle with a diameter of ~ 270 microns under high pressure (2000 psi) (a single spraying route is referred to as a cycle). A total of 5 cycles were used for the whole process. The exfoliation occurs due to the shear stress generated at the nozzle's edges. [86]. Finally, the resultant black dispersion was centrifuged at 5000 rpm for 30 min to remove thick and unexfoliated flakes, and the supernatant containing the FLG flakes was collected. Thermogravimetric analysis was used to estimate the concentration of the FLG flakes in the dispersion, which was found to be 1.4 mg/mL. The entire procedure for realizing the dispersion is schematically shown in Fig. 1a. Since the graphene flake dispersion was produced in water with the aid of surfactants, we proceeded to exchange the solvent from water to ethanol to wash the sample and remove any residues of the surfactants. To this end, after centrifugation, 20 mL of the dispersion was vacuum filtered through a PTFE membrane (47 mm diameter, 220 nm pore size), after which the exfoliated flakes were collected. The membrane was ultrasonicated in 30 mL of ethanol (15 min, room temperature) to redisperse the flakes. The obtained dispersion (with a concentration of 0.8 mg/mL) was used to characterize the flakes before preparing the composite paste, as explained in the following sections.

2.3. Composite paste preparation

Starting from the FLG dispersion in water, a rotary evaporation process (50 °C and 80 mbar) was used to remove the water. The resulting powder was treated several times with acetone to remove residues from the surfactants/additives and was finally heated at 60 °C (for 2 h in an oven) to remove the acetone. The FLG flake powder was used to prepare a composite paste. 7 wt% of FLG powder and 2 wt% of carbon black were mixed and added to 1 wt% of gum arabic dissolved in 89.5 wt% of Cyrene. Then, 0.5 wt% BYK ES-80 was added. The composite was stirred overnight (600 rpm, room temperature).

2.4. Materials characterization

2.4.1. Raman spectroscopy

50 μL of the graphene dispersion in ethanol were drop cast onto glass substrates (1 × 1 cm^2) and dried at 60 °C for 10 min. Measurements were performed with an ALPHA300 R Confocal Raman Microscope (WITec) using 532 nm laser light for excitation at room temperature. The laser beam was focused on the sample with 50x and 100x lenses (Zeiss). Single acquisitions were performed using a 600 g/mm grating and a P_{Laser} below 2 mW to minimize localized heating and damage to the sample.

2.4.2. Scanning electron microscopy (SEM)

50 μL of the graphene dispersion in ethanol were drop cast on a Si substrate (1 × 1 cm^2) and dried at 60 °C for 10 min. Images were acquired using an FEI Quanta 650 FEG with a cold field emission electron source using acceleration voltages between 5 kV and 10 kV at a 10 mm working distance in a high vacuum.

2.4.3. Transmission electron microscopy (TEM)

20 μL of the graphene dispersion in ethanol were drop-cast on Cu grids (200 mesh, covered with lacey carbon) and allowed to dry at 80 °C for 30 min. The structure of the graphene flakes was investigated using a JEOL 2100 system operated at 200 kV.

2.4.4. X-ray photoelectron spectroscopy (XPS)

50 μL of the graphene dispersion in ethanol were drop-cast on Si substrates (1 × 1 cm^2) and dried at 40 °C for 30 min (then stored in a desiccator). XPS spectra were acquired with an ESCALAB 250 XI (Thermo Fisher Scientific, Source: Al K_α 1486.6 eV, 650 μm spot size, Pass energy: 40 eV with hemispherical analyzer) system with an analysis chamber maintained in ultrahigh vacuum (UHV ~ 5 × 10^{-10} mbar) conditions. A dual beam consisting of Ar+ ions (0.5 KeV) and electrons (0.5 KeV) was used to clean the surface of the graphene flakes over a four mm^2 area during the measurements.

2.4.5. Atomic Force Microscopy (AFM)

50 μL of the graphene dispersions in ethanol were drop-cast on Si

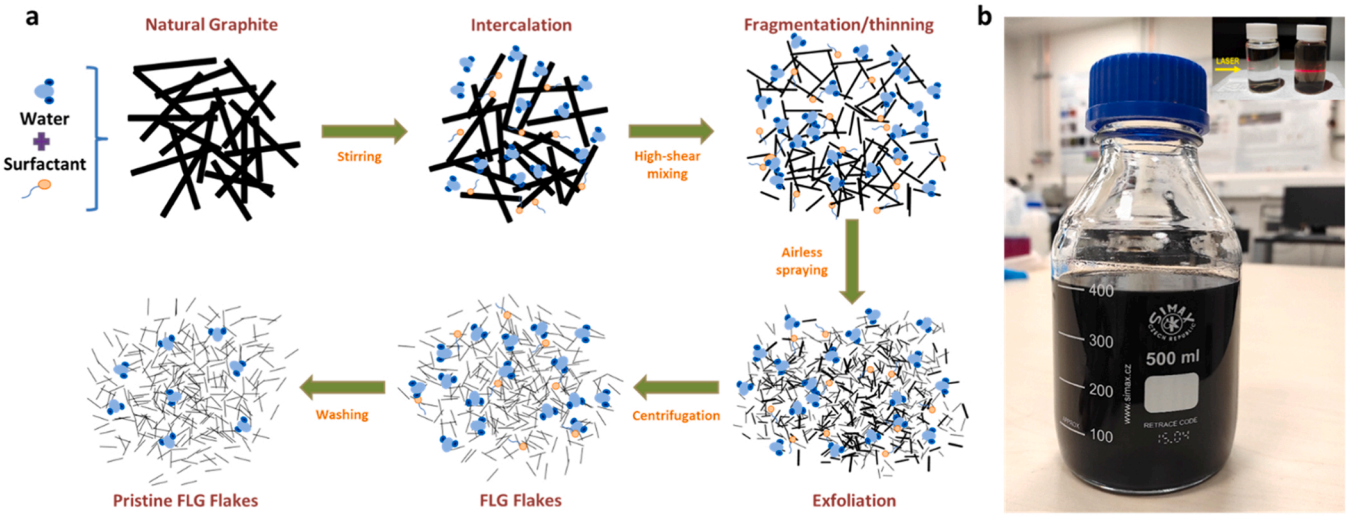

Fig. 1. Preparation of large volumes of homogeneous FLG flake dispersions for graphene-based applications. (a) Schematic depiction of the FLG preparation process combining HS and HP exfoliation. (b) The colloidal graphene dispersion in water is homogeneous, as confirmed by the Tyndall effect (inset).

substrates (1 × 1 cm^2) and dried at RT. Afterwards, the samples were heated on a hot plate at 100 ºC for 2 h. AFM was utilized to measure the size and thickness of the graphene flakes. The samples were characterized on a Bruker Dimension ICON instrument in tapping mode, using Al-coated Si tips (with resonant frequency of 300 kHz).

2.4.6. Thermogravimetric analysis (TGA)

TGA was used to determine the solid content in the paste. 50 mg of the paste was collected in a crucible and analyzed with a Model TGA 1 (Mettler Toledo) in Ar and air atmospheres (flow rate of 25 mL/min). An initial 10 min purge was run at 30 °C under the selected atmosphere (flow rate of 50 mL/min) at a heating rate of 10 °C/min. The data were analyzed, and the mass loss and degradation temperature were calculated using Origin software.

2.4.7. Rheology

The rheological properties of the paste were assessed via rotational shear tests using an Anton Paar MCR302 rheometer equipped with a 50 mm plate-plate geometry. Measurements were carried out in shear-controlled mode at 25 °C. The temperature was carefully controlled using two different Peltier cells (one dedicated cell for each plate). The shear rate varied between 0.1 and 100 s-1, acquiring 1 point every 10 s (for 50 data points). Measurements were repeated in triplicate.

2.4.8. Device fabrication

EMI shielding coatings, mSCs, and strain sensors were fabricated with the composite paste using the mask-assisted blade coating method. Customized masks were fabricated by laser cutting (Widlaser LS1390 Plus, 10% laser power, 10 mm/min scanning speed). Both the mSC and EMI samples were fabricated on a flexible PET substrate (75 μm), while the strain sensors were fabricated on a textile. **mSC:** For the mSC electrodes, the mask was transferred to a 75 μm thick flexible polyethylene terephthalate (PET) substrate. The paste was poured on the mask, squeezed using a glass rod, and dried under ambient conditions. The mask was removed, and the mSC electrodes were dried at 80 °C overnight. The final structure of mSCs consists of 10 fingers 1 mm wide that form an interdigitated configuration with a 600 μm spacing between the fingers. The device's active area and mass loading were 1.6 cm^2 and 4.4 mg, respectively. A drop of gel electrolyte (100 mg/mL PVA in water and 20% H_2SO_4) was cast on top of the active area of the mSC plate and allowed to dry at room temperature, thus obtaining a device ready for performance evaluation. The stack assembly was achieved by connecting single cells with Ag conductive paint (SPI supplies). **EMI shielding coatings**: A mask with a 7×7 cm^2 square pattern was used to blade-coat the paste on the PET substrate. This step was repeated several times to increase the coating thickness until the desired thickness was reached (as measured by a digital micrometer). **Strain sensors:** A customized mask was used to blade-coat the paste on the textile substrate, defining a closed conductive pattern (with an "H" shape of 13 × 9 mm, a total length of 50 mm and a width of 0.5 mm). Ni paste was used to connect the ends of the graphene sensor to the electrical wires.

2.5. Device characterization

2.5.1. Electrical conductivity measurements

The surface conductivity of the coatings was measured at room temperature using a custom-made spring-loaded 4-point probe connected to a source meter (Keithley 2400) operating at a constant DC of 0.2 mA and a compliance bias of 2.1 V. The surface conductivity was calculated from an average of 15 individual measurements in the central region of each sample.

2.5.2. mSC electrochemical characterization

The electrochemical response of the symmetric cells was determined by galvanostatic charge—discharge (GCD), cyclic voltammetry and electrochemical impedance spectroscopy (EIS). EIS tests were executed with a 10 mV rms potential perturbation around the OCP, in the frequency range from 100 kHz to 10 mHz, and with 10 points per decade with a logarithmic distribution. The electrochemical stability of the cells was assessed by GCD for 10000 cycles. All the electrochemical experiments were executed inside a Faraday cage at room temperature using a Gamry 1010E potentiostat.

2.5.3. Shielding effectiveness measurements

The most important criterion for measuring the shielding performance of a material is the shielding effectiveness (SE), defined as the logarithmic ratio of the transmitted power when a shield is present to the power transmitted without the shield [87]. Experimentally, the reflected and transmitted waves can be measured with a two-port VNA and represented by complex scattering parameters (S-parameters S_{11}, S_{12}, S_{21}, and S_{22}). According to the calculation theory [88], the law of energy conservation is considered when an incoming wave interacts with a material. The incident power is split into reflected power ($R = |S_{11}|^2$), absorbed power (A), and transmitted power ($T= |S_{21}|^2$), and the sum of all the powers must be balanced (R+A+T=1).

The total SE (SE_T), expressed in dB, can be calculated as the sum of the reflection loss (SE_R), the absorption loss (SE_A), and multiple reflection loss (SE_M), where generally the latter has a negligible contribution when the loss via absorption is greater than 15 dB or when the material thickness is greater than the skin depth [89]:

$$\boldsymbol{SE_T} = \mathbf{10log_{10}}\left(\frac{\boldsymbol{P_I}}{\boldsymbol{P_T}}\right) = 10\log_{10}\left(\frac{1}{T}\right)\boldsymbol{SE_R} + \boldsymbol{SE_A} + \boldsymbol{SE_M} \quad (1)$$

Where P_I represents energy of the incident wave and P_T represents energy of the transmitted wave

$$\boldsymbol{SE_R} = \mathbf{10log}\left(\frac{\boldsymbol{1}}{\mathbf{1-R}}\right)\mathbf{10log}\left(\frac{\boldsymbol{1}}{\mathbf{1-|S_{11}|^2}}\right) \quad (2)$$

$$\boldsymbol{SE_A} = \mathbf{10log}\left(\frac{\mathbf{1-R}}{\mathbf{T}}\right)\mathbf{10log}\left(\frac{\mathbf{1-|S_{11}|^2}}{\boldsymbol{|S_{21}|^2}}\right) \quad (3)$$

The EMI shielding of the planar samples was measured on a vector network analyzer (VNA, R&S ZNB4) in the frequency range of 30 MHz – 3.2 GHz, adapting the procedure from ASTM D 4935. Before the measurements, all the cables and connectors were tightened using a torque wrench, and the equipment was calibrated using the ZN Z170 calibration kit.

2.5.4. Electromechanical characterization of the strain sensors

The stress—strain curves and destructive tests were performed on a universal testing machine (AGX™-V, Shimadzu Corporation) using a linear speed of 0.6 mm/min. The long-term cycling test (uniaxial stress) was performed using a Thorlabs stage (XR25/M) with a DC servo actuator (Z825B) and the respective controller (KDC101). The electrical resistance was measured during the mechanical tests with a digital multimeter (Agilent 43410 A). For heartbeat acquisition, the sensor was driven at 1 μA with a current source (Keithley 2400 Sourcemeter), and the signal was acquired in the time domain with an oscilloscope (T3DSO1204, Teledyne LeCroy). The only signal processing used was a low-pass filter with a cutoff frequency of 40 Hz.

3. Results and discussion

Large volumes of homogenous and stable dispersions of FLG flakes in water were produced by combining HS and HP exfoliation, as described in Section 2.2 and depicted in Fig. 1a. To overcome the long processing time required by HS mixing, we combined this process with high-pressure (HP, in the ~ 1.4–2.0×10^7 Pa range) airless spray exfoliation in a two-step process [90]. In standalone HP exfoliation, bulk graphite is usually soaked for several days (up to seven) to weaken the vdW

interactions among the layers and facilitate exfoliation [86]. This soaking step is time-consuming for industrial production but can be avoided by the first step of HS mixing. Our method allowed the production of stable graphene dispersions in water. Fig. 1b shows a real-time photographic image of graphene dispersions in water. The inset in Fig. 1b shows the Tyndall effect within the dispersion, confirming its colloidal nature.

Raman spectroscopy was used to study the thickness, lateral size, defect density, and electronic doping properties of the FLG flakes. A representative spectrum of the graphene flakes compared to that of the original bulk graphite used for the exfoliation process is shown in Fig. 2a. The D band in both spectra is centered at ~1352 cm^{-1}.

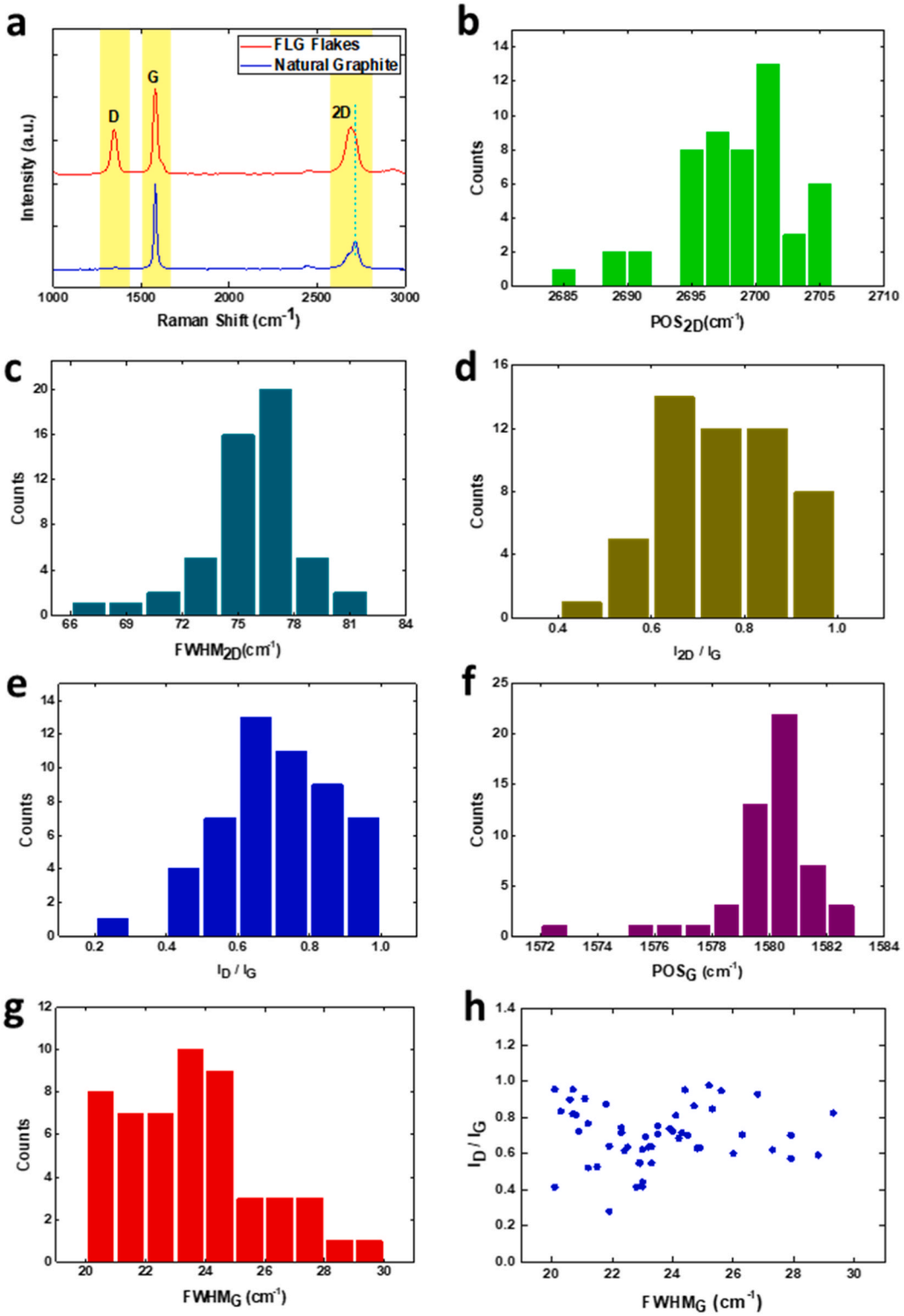

Fig. 2. Raman spectra representative of graphene flakes: (a) Raman spectroscopy analysis comparing the graphene flakes to bulk graphite revealing redshifted G and 2D bands and an increased I_D/I_G ratio, indicative of thinning to few-layer graphene. Distribution of b) Pos_{2D}, c) $FWHM_{2D}$, d) the I_{2D}/I_D ratio, e) the I_D/I_G ratio, f) Pos_G, g) $FWHM_G$, and h) I_D/I_G ratios as a function of the $FWHM_G$.

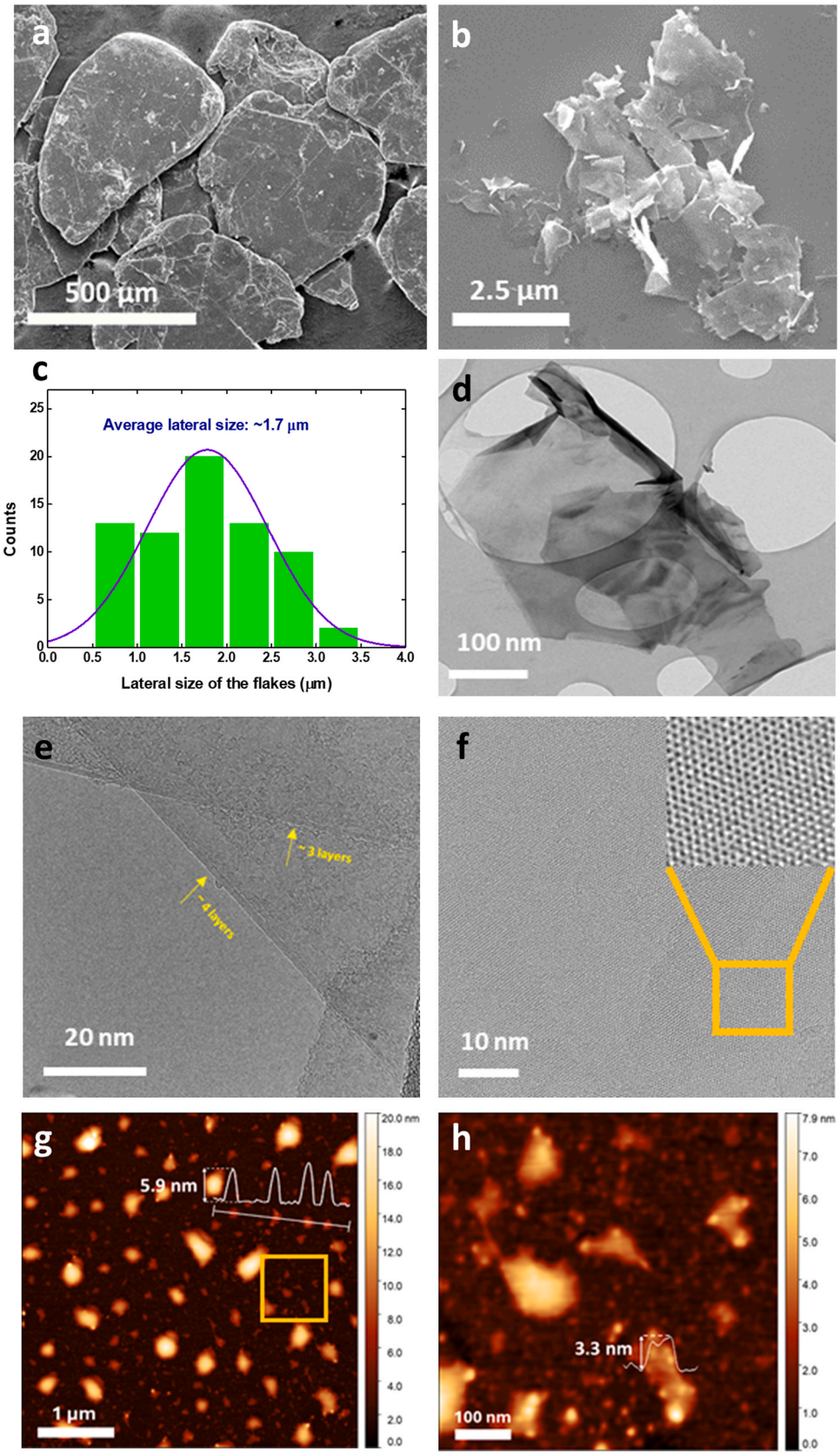

Fig. 3. Microscopic characterizations of the materials. (a) SEM image of the bulk natural graphite, demonstrating the mm-size of the graphite grains. (b) SEM image of the FLG flakes, which have sharp and polygonal shapes and lateral sizes in the µm range. (c) Statistical analysis of the lateral size, which has a Gaussian distribution. (d) TEM image of individual FLG flakes. (e) HRTEM image of the edge of the flakes showing a thickness within the few-layer range (i.e., below five layers). (f) HRTEM image showing the regular lattice structure of the flakes (with the enlarged region in the inset). (g) AFM micrograph of the graphene flakes deposited on a Si substrate, showing an even and narrow distribution of sizes. (h) Magnified view of the 500×500 nm area highlighted in the yellow square in (g), showing the details of the flake structure.

Moreover, the G and 2D bands of the graphene flakes are redshifted with respect to those of natural graphite (~1577 *vs.* ~1581 cm^{-1}, ~2695 *vs.* ~2719 cm^{-1}) [91]. The I_D/I_G ratio in the graphene flakes increases substantially (0.52 *vs.* 0.02), as does the I_{2D}/I_D to a minor extent (0.57 *vs* 0.32). The redshift and symmetrical broadening of the 2D peak, along with the increased intensity, confirm that the graphite has thinned down to few- or multi-layer flakes [92]. The I_D band broadening points to most flakes with sub-μm lateral sizes rather than a proliferation of defect sites. On the other hand, the 2D band provides information about the number of layers in the few-layer range [93–95]. We collected Raman spectra from 60 individual flakes to conduct an accurate statistical analysis of the main spectral features. From the distributions in the histograms of Figs. 2b and 2c, Pos_{2D} is centered at ~2695 cm^{-1}, while its full width at half maximum ($FWHM_{2D}$) is centered at ~75 cm^{-1}. These two distributions are remarkably narrow, indicating atomically thick flakes with small variations within the batch [37]. The I_{2D}/I_G and I_D/I_G ratios are centered at ~0.75 and ~0.65, respectively (Fig. 2d and e). The I_{2D}/I_G range is consistent with the thickness of mono- to few-layer graphene, while the I_D/I_G values can be attributed to the sub-μm size of the flakes rather than the high density of structural defects, as typically observed in LPE samples [38]. Pos_G is centered at ~1580 cm^{-1}, while its $FWHM_G$ is centered at ~24 cm^{-1} (Figs. 2f and 2g), as also expected. Additional information can be found by plotting the I_D/I_G ratio *vs* $FWHM_G$, which is also an indicator of the crystalline quality and defect density of graphene crystals. Conventionally, defected samples would show a correlated increase in both $FWHM_G$ and I_D/I_G ratio. The plot in Fig. 2h, instead, shows no apparent correlation between the two indicators. This suggests that the major contribution to the D mode stems from the irregular edges of the flakes, rather than a high defect density within their basal planes, as in the case of crystalline, sub-μm flakes. Overall, the observed spectral features confirm the efficiency of the exfoliation process in producing FLG flakes with small sizes, narrow size distribution, and low defect density [37,96].

Fig. 3a and b show SEM images of the natural graphite used for exfoliation and the resulting FLG flakes deposited on a Si substrate, respectively. The flakes appear exfoliated as expected, although they are partially reaggregated on Si due to the deposition process (and drying) [96]. We performed a statistical analysis of the lateral size of the flakes by acquiring TEM images and measuring the sizes of 70 individual flakes (Fig. 3c). The size histogram follows a Gaussian distribution centered at 1.7 μm. Such analysis might provide a slight overestimation due to the agglomeration of flakes on the TEM grid, which complicates the exact individuation of the flakes' margins. In Fig. 3d, we show a representative image with clearly identifiable flakes, which point at a lateral size in the sub-μm range. The image further confirms the atomic thickness of the FLG flakes, which are completely transparent to the electron beam. A careful examination of the edge of the flakes (obtained by tilting the samples under an electron beam) confirmed the few-layer thickness of the flakes (Fig. 3e). The HRTEM image in Fig. 3f highlights the crystalline structure of the flakes, with no observable defects. The AFM micrographs in Fig. 3g and h confirm the main flake morphology observed by TEM, with lateral size in the sub-μm range and thickness up to a few nm.

X-ray photoelectron spectroscopy (XPS) was performed to determine the chemical composition of the exfoliated flakes. In Fig. 4a, the survey spectrum of the bulk graphite used for the exfoliation process shows the main C peak and a minor O peak, as expected. The spectrum of the FLG flakes exfoliated in water shows analogous C and O peaks, as well as the appearance of Na-related peaks due to residues of the sodium deoxycholate ($C_{24}H_{39}NaO_4$) surfactant used to promote the exfoliation process in water. After the solvent exchange process (where the flakes are collected and redispersed in ethanol; see Section 2.2), the Na peaks disappear, confirming the effective removal of any residue. This situation is confirmed by the detailed analysis of the FLG samples in Fig. 4b and c. Both C1s spectra show main sp^2 and sp^3 hybridized carbon components (284.1 and 284.6 eV) and three components related to C-O-C, C-O, and C═O oxides (at 285.3, 286.7, and 288.5 eV, respectively), as typically expected in exfoliated flakes [97]. The spectrum of the sample exfoliated in water (Fig. 4b) has a more intense sp^3 hybridized component than the sp^2 hybridized component (51% *vs* 16% weight of the deconvoluted C1s spectrum). Of the other three oxide-related components, C-O-C is the most significant (26%), probably because sodium deoxycholate residues partially cover the flake surface. In general, FLG flakes prepared by airless-spray processes may present a high density of superficial/edge defects, which could be saturated by oxygen-containing functional groups (*e.g.*, hydroxyl and epoxy groups, possibly provided by the additive/surfactant molecules used). The situation changes after the exchange of ethanol (Fig. 4c): here, the sp^2 hybridized component is the most intense (50.7%), while the oxide-related components are substantially reduced.

An electrically conductive composite paste was formulated as described in Experimental Section 2.3. A photograph of the prepared paste is shown in Fig. 5a. By considering the weight of the components used to make the formulation, we calculated the total solid content (*i.e.*, percentage of graphene and carbon black) as ~ 9%. TGA of the paste was performed in both air and N_2 atmosphere, and the resultant weight loss curves are plotted in Fig. 5b. Most of the mass loss (88.5% wt) occurs between 80 °C and 230 °C. The latter temperature corresponds to the boiling point of Cyrene, thus indicating that most of the loss in this range can be attributed to the evolution of the solvent. Above 230 °C, the mass loss under the N_2 atmosphere was negligible. The residue corresponds to the solid content (FLG and carbon black) in the paste, in good agreement with the weight ratios in the formula described in Section 2.3. The flow properties of the paste were investigated by measuring the dependence of the apparent dynamic viscosity on the applied shear rate at 25 °C. Fig. 5c shows the obtained viscosity curve of the paste, highlighting an explicit non-Newtonian behavior in the investigated shear rate range (between 0.1 and 100 s^{-1}). This behavior is strongly shear thinning, as

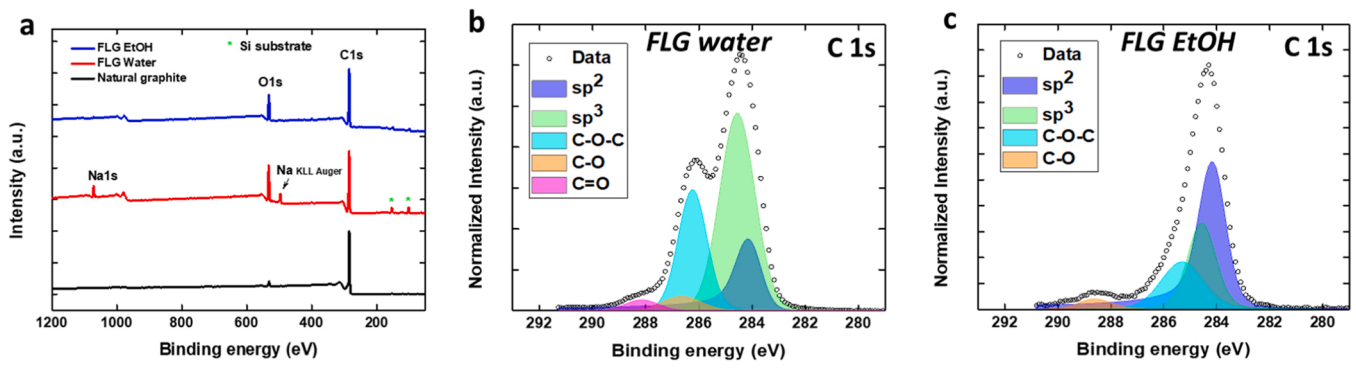

Fig. 4. XPS spectra of the samples deposited on Si. (a) Survey spectra of natural graphite, exfoliated flakes (FLG water), and exfoliated flakes after solvent exchange from water to ethanol (FLG EtOH). Deconvoluted C1s spectra of (b) FLG water and (c) FLG EtOH.

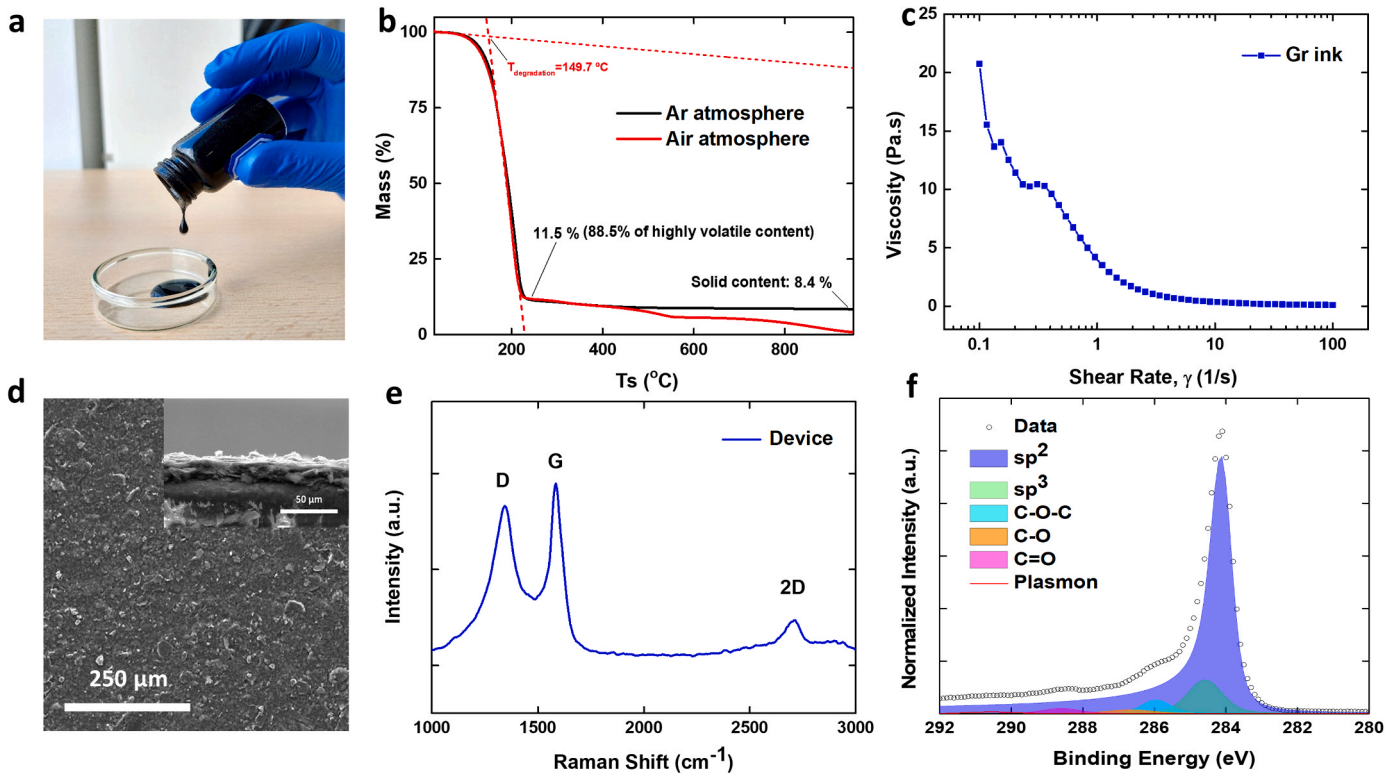

Fig. 5. Characterization of the graphene conducting paste. (a) Real-time photograph of the formulated FLG-based paste with high viscosity. (b) TGA analysis of the paste, showing weight loss attributed to solvent evolution and residue corresponding to FLG and carbon black content. (c) Viscosity curve highlighting the non-Newtonian, shear-thinning behavior of the paste. (d) SEM image of the coating on a PET substrate, demonstrating a uniform continuous coating with no pinholes. The inset shows the cross-sectional image. (e) Raman and (f) XPS analysis confirming the graphitic nature of the FLG-based coating.

demonstrated by the wide span in apparent viscosity, starting from ~ 20 Pa•s for the low shear rate range down to 0.1 Pa•s for the highest shear region. After the paste was stored at room temperature for six months, no sedimentation of the solid content occurred. Importantly, for these applications, over the same time span, the paste never dried, probably due to the addition of the minimal amount of Cyrene, a high boiling point solvent. A planar SEM image of the coating on the PET substrate (as described in the device fabrication section) is shown in Fig. 5d, and the corresponding cross-sectional image is shown in the inset. A uniform continuous coating was observed with no pinholes. The FLG flakes and carbon black particles are well connected within the gum arabic matrix, thus favoring percolation. Raman and XPS data for the coating are also given in Figs. 5e and 5f, respectively. XPS analysis of the C1s region of the paste (Fig. 5f) revealed a main sp^2 peak and few secondary components related to sp^3-coordinated carbons and small amounts of oxide. With respect to the FLG flake spectrum, the main difference is the significant reduction in the C-O component and the concomitant increase in the sp^3-related peak. The C-O-C component is minimal in both samples and appears to be downshifted in the flake spectrum (probably due to weak surface oxidation). These results show no other elemental traces in the coating, confirming the carbon-based nature of the composite [98–100].

3.1. Flexible microsupercapacitors

Graphene-based mSCs were fabricated as described in Section 2.3. The device architecture consists of 10 fingers 1 mm wide, forming a planar interdigitated configuration with a 600 µm spacing between the fingers (Fig. 6a). The active area and mass loading of the device were 1.6 cm^2 and 4.4 mg, respectively. The electrochemical response of the mSCs was evaluated through cyclic voltammetry and GCD tests in a potential window between 0.0 and 0.8 V. The percentage contribution of the charge storage on the inner and outer surfaces of the electrodes was estimated according to the Trasatti method [101]. The areal capacitance, C_A, was calculated from the discharge curves according to the equation:

$$C_A = \frac{i.t_d}{A.\Delta E} \tag{4}$$

where i is the applied current, t_d is the measured discharge time, A is the total area of the electrodes in contact with the electrolyte, and ΔE is the potential range during the discharge experiments. The energy and power density were calculated through the following equations:

$$E_A = \frac{1}{2} C_{cell} V^2 \tag{5}$$

$$P = \frac{E_A}{t_d} \tag{6}$$

where E_A is the areal energy density, C_{cell} is the capacitance of the cell, V is the potential window, and t_d is the discharge time. The cyclic voltammograms of the cells for different anodic limits at 50 mV s^{-1} are shown in Fig. 6b, and those at different scan rates are shown in Fig. 6c. As expected for a carbon-based material, the voltammograms are almost rectangular without redox peaks, indicating capacitive behavior. The inner surface contributes 90.7% of the total charge. The GCD curves obtained at different current loads (40, 70, 100, 150, 200, and 250 µA cm^{-2}) are shown in Fig. 6d. These curves exhibit a nearly triangular shape with a low ohmic drop and a Coulombic efficiency close to 100%. The cells presented areal and volumetric capacitances of 6.16 mF cm^{-2} and 2.46 F cm^{-3}, respectively, at a current density of 40 µA cm^{-2} (Fig. 6e). The maximum energy density was 209 µWh cm^{-3} at a power density of 6.25 mW cm^{-3}, as shown by the Ragone plot depicted in Fig. 6g. The developed supercapacitors performed well compared to

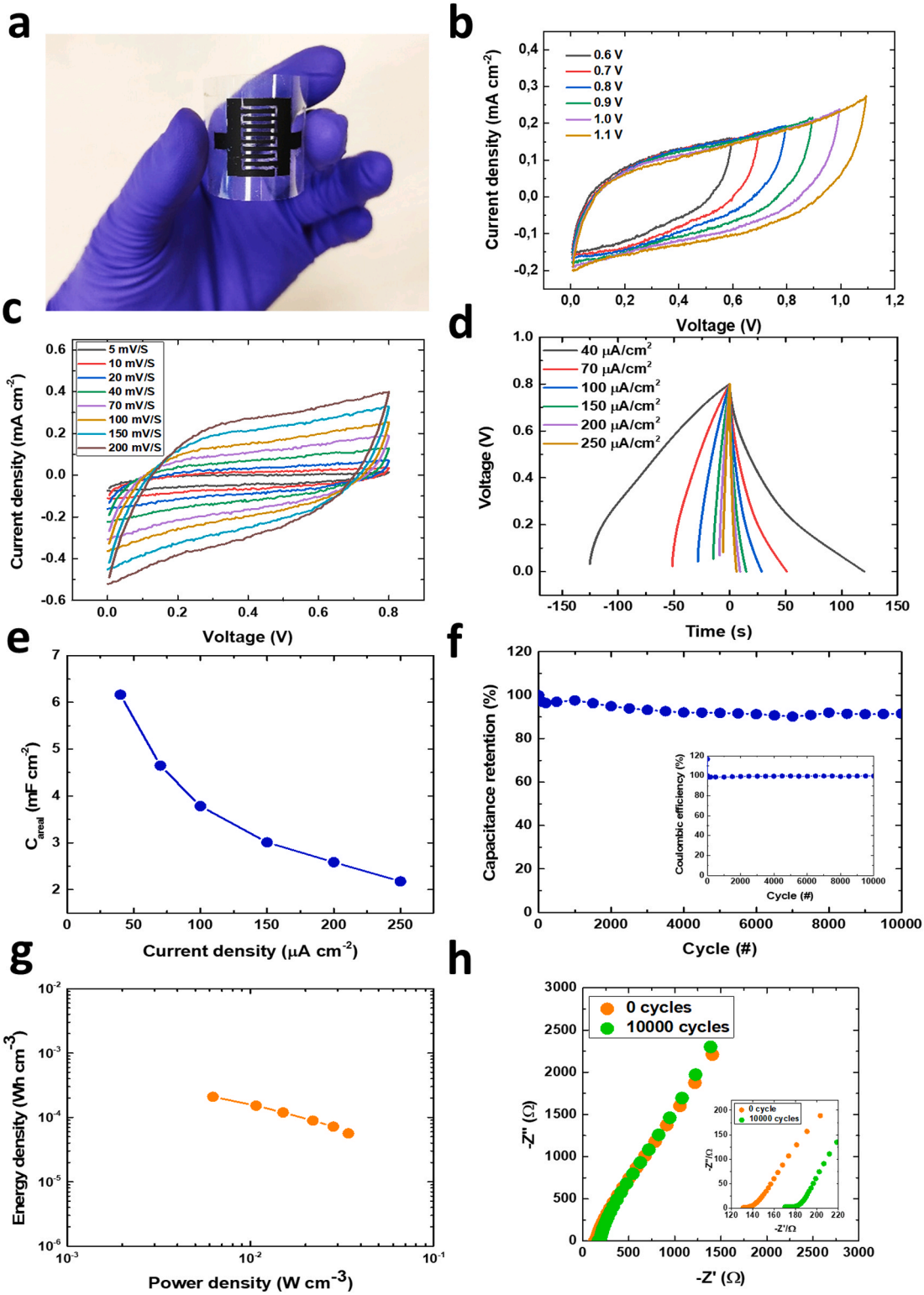

Fig. 6. Performance evaluation and characterization of graphene-based mSCs. (a) A flexible mSC (with a total area of 2.1×2.1 cm^2) consisting of an interdigitated electrode configuration with 10 fingers (1 mm wide, 600 μm spacing). (b) Cyclic voltammograms of the supercapacitor cells at different anodic limits, measured at a scan rate of 50 mV s^{-1}. (c) Cyclic voltammograms at various scan rates. (d) Galvanostatic charge—discharge (GCD) curves obtained at different current densities. (e) Areal capacitance as a function of current density. (f) Rate capability and coulombic efficiency (inset) of the device over 10,000 GCD cycles. (g) Ragone plot displaying the energy density as a function of the power density. (h) Electrochemical impedance spectroscopy (from 100 kHz to 10 mHz) results before and after the GCD stability test.

previous work that followed a similar methodology. For instance, screen-printed graphene-based supercapacitors delivered 1.324 mF cm^{-2} at 12.5 μA cm^{-2} [24] and 1.0 mF cm^{-2} at 5 mV s^{-1} [102]. Graphene-based mSCs prepared through other methods, such as full inkjet printing [103] or flash foam stamp-inspired techniques [104], previously exhibited areal capacitances of 0.7 and 4.02 mF cm^{-2}, respectively, at 10 mV s^{-1}. Vertical graphene-based supercapacitors grown by chemical vapor deposition presented an areal capacitance of 1.06 mF cm^{-2} at a discharge current density of 0.1 mA cm^{-2} [105]. The mSCs exhibited good rate capability (Fig. 6e) and a coulombic efficiency near 100% (inset of Fig. 6f), which was determined by the charge—discharge transient ($t_{discharge}/t_{charge}$). The device also showed an excellent capacitance retention of ~ 91.5% after 10000 GCD cycles under a current pulse of 250 μA cm^{-2} (Fig. 6f). The stability test led to a slight increase in the resistivity of the device, as shown in the impedance spectra (Fig. 6h).

The mechanical flexibility of the cells was evaluated through cyclic voltammetry at 50 mV s^{-1} under different bending degrees (0, 30, 45, 60, and 90°, corresponding to radii of 4, 2.7, 2 and 1.3 cm), as shown in Fig. 7a. The bending of the electrodes did not decrease the performance of the supercapacitor, as shown by the almost coincident voltammograms. In contrast, the device capacitance slightly increased with increasing bending angle (Fig. 7b). This is probably due to the formation of defects that expose the active material, thus enhancing the area accessible to the electrolyte. Additionally, the devices sustain the deformation well, as no deadhesion or collector response is observed. To demonstrate the possibility of modularizing these cells with adjustable outputs (voltage and capacitance), a combination of two cells in series (denoted as 2S1P) and in parallel (1S2P) and a stack with two rows of two cells in parallel (2S2P) were characterized through cyclic voltammetry (CV) at 50 mV s^{-1}, GCD at 0.1 mA cm^{-2}, and EIS, as shown in Figs. 7d, 7e and 7f, respectively. Combining two cells connected in parallel (1S2P) led to an increase in the nominal capacitance of the

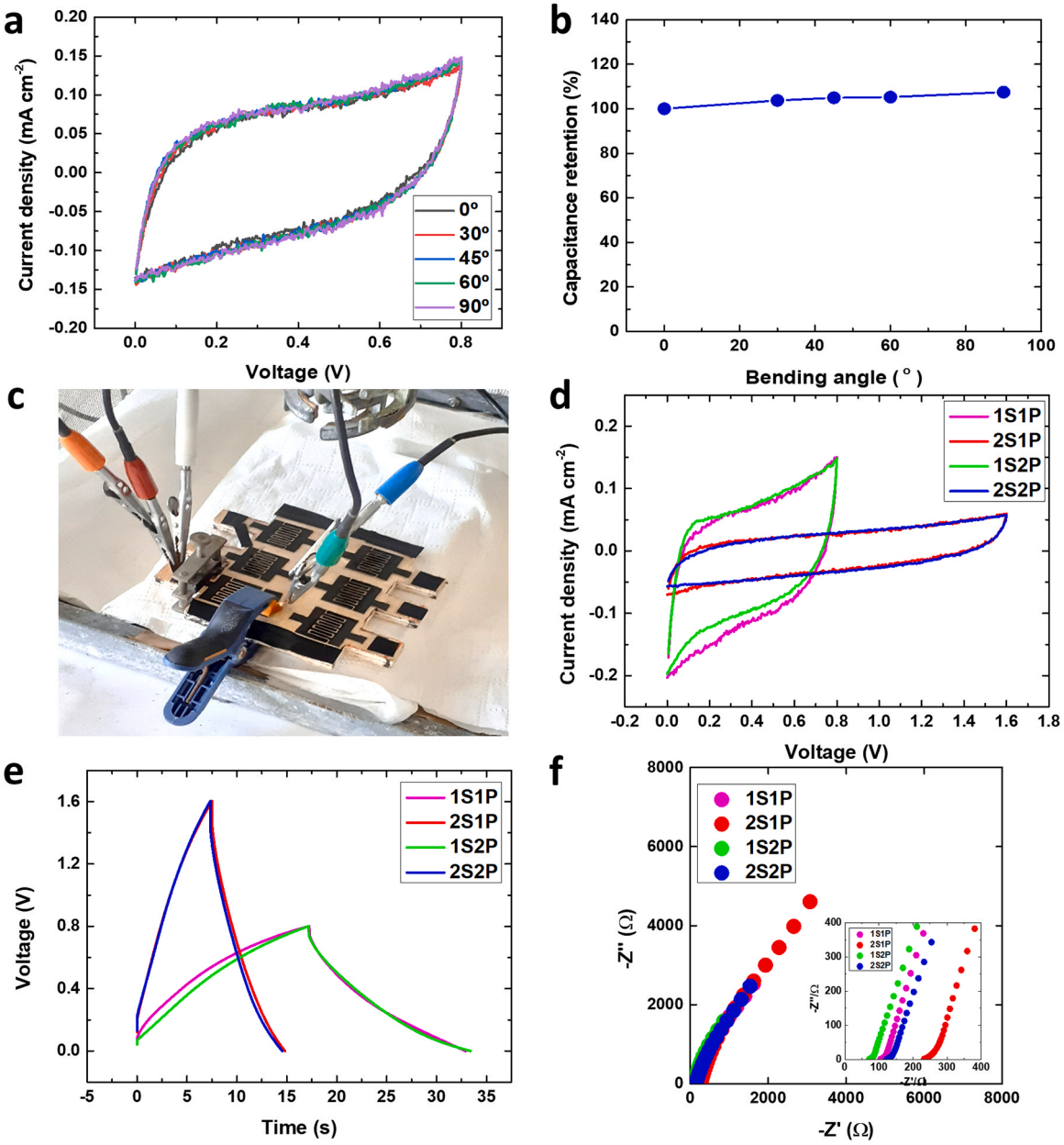

Fig. 7. Mechanical flexibility and modularization of supercapacitor cells. (a) Cyclic voltammograms of supercapacitor cells at 50 mV s^{-1} in different bending states. (b) Capacitance retention during bending tests. (c) Photo of the stack characterization apparatus. (d) Cyclic voltammograms at 50 mV s^{-1}. (e) Galvanostatic charge—discharge (GCD) tests at 0.1 mA cm^{-2}. (f) Electrochemical impedance spectroscopy (EIS) study of stacks with different configurations.

device of ~ 87%. It promoted a decrease in impedance (Fig. 7f) compared to that of a single cell. As expected, connecting two cells in series (2S1P) promoted an increase in the potential window equal to the sum of the individual cells. However, the nominal capacitance decreased by 34%, and the overall impedance increased. The 2S2P stack presented a 33% increase in capacitance and a doubling of the working window compared to those of 1S1P. The coincident voltammograms and chronopotentiograms for stacks with the same number of cells in series but different numbers of rows in parallel (Figs. 7d and 7e) show that the integration of several cells in different configurations does not significantly affect the excellent performance evidenced by a single cell, which demonstrates the ability of these electrodes to be modularized.

3.2. EMI shielding coatings

To realize efficient EM screening, our graphene paste was iteratively deposited on PET to realize coatings (Fig. 8a) with increasing thickness, as described in Experimental Section 2.5. The samples were mounted in a brass waveguide assembly connected to a VNA setup for measuring the S-parameters. In Fig. 8b, the average shielding effectiveness values are plotted against the coating thickness (see Experimental section 2.6 for the definitions). These values are also presented in Table 1, along with the sheet resistance and conductivity of the coatings.

Table 1
Overview of the graphene-based coating thickness, sheet resistance, conductivity, and average SE.

Sample	Thickness (μm)	R_{sheet} (Ω/sq)	$\sigma_{surface}$ (S/m)	SE_{Rn} (dB)	SE_{An} (dB)	SE_T (dB)
A	11.6 ± 3.5	127 ± 65	680 ± 400	2.1 ± 0.6	6.0 ± 1.0	8.1 ± 1.1
B	19.1 ± 7.7	40 ± 20	1320 ± 840	3.6 ± 0.8	9.5 ± 1.6	13.1 ± 2.0
C	33.2 ± 4.4	16.4 ± 1.8	1840 ± 310	7.4 ± 1.4	12.6 ± 1.5	19.9 ± 2.1
D	47.8 ± 9.0	7.1 ± 2.0	2940 ± 1000	8.3 ± 1.9	14.4 ± 2.2	22.7 ± 1.8

By analyzing the plot and the table, it is apparent that the conductivity scales linearly with the coating thickness, as does the total SE. However, the increase in total SE is primarily due to reflection loss (SE_R), which can be written as [106,107]:

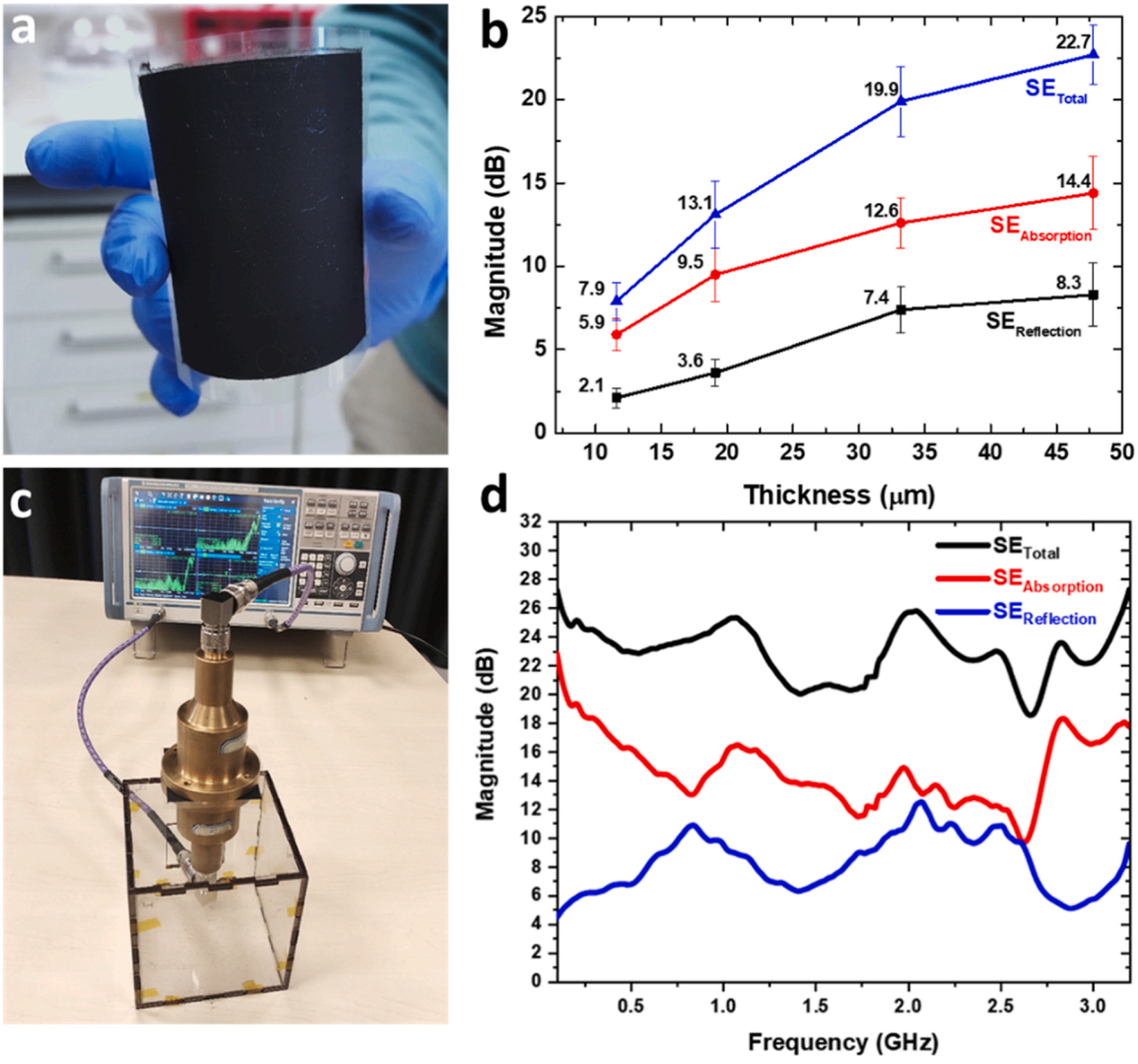

Fig. 8. Graphene-based EMI shielding coatings on PET substrates. (a) Photographic image of graphene-based paste coated on PET. (b) Average SE values due to reflection (SE_R, black plot), absorption (SE_A, red plot), and total absorption (SE_T, blue plot) of graphene-based coatings with different thicknesses. (c) The setup used to measure the S-parameters of the produced samples. The sample is placed between two brass waveguides connected to a 50-Ohm attenuator and the VNA. (d) SE_R, SE_A, and SE_T vs frequency for sample D (300 MHz to 3.2 GHz frequency range).

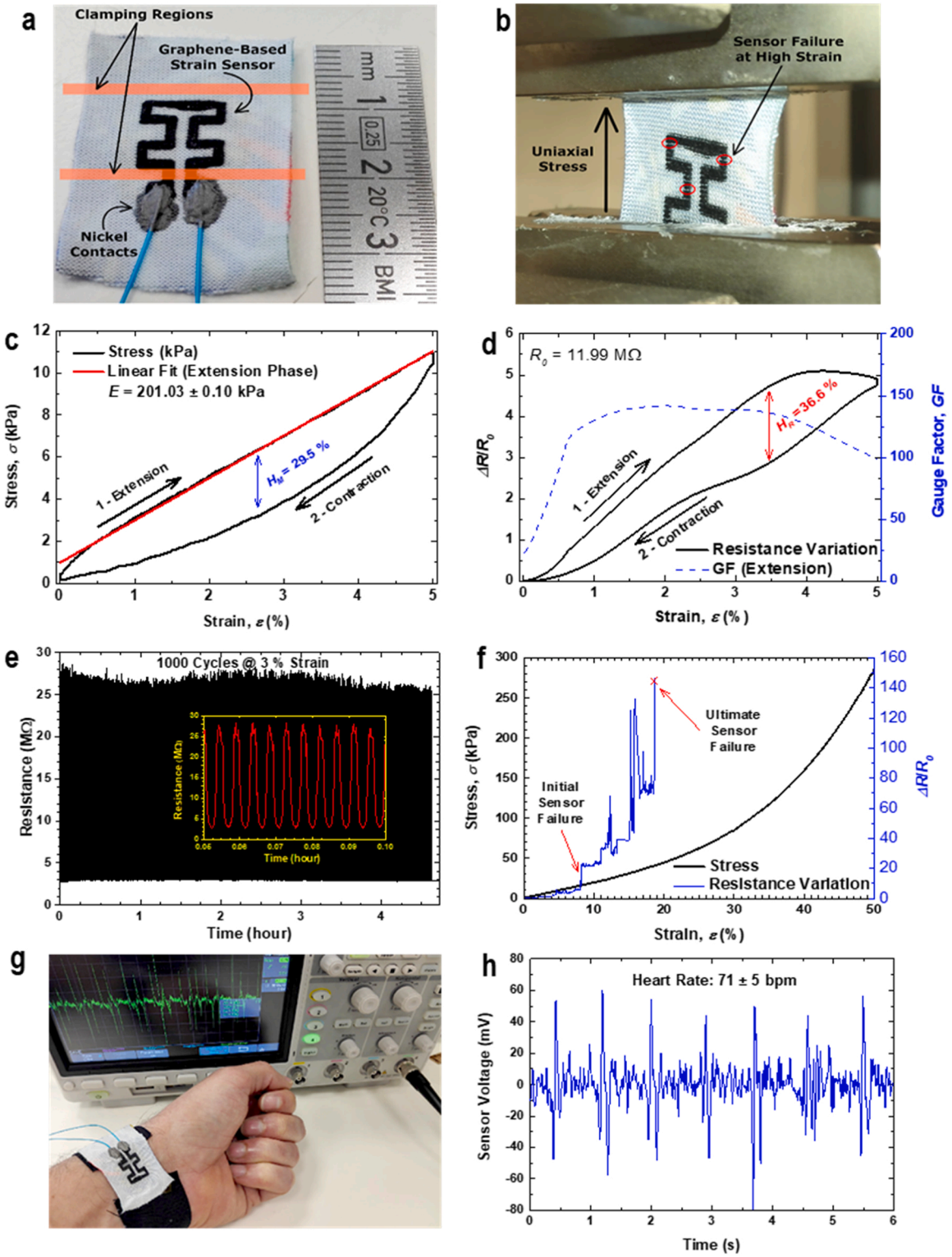

Fig. 9. Textile strain sensor characterization. (a) Photograph of the device showing the electrical connections. (b) Strain sensor mounted on a universal testing machine for stress—strain characterization and destructive tests (cracks formed on the sensor for ε > 8%). (c) Mechanical characterization of the sensor (stress vs. strain). (d) Resistance variation and gauge factor as a function of strain. (e) Long-term cycling of the sensor at ε = 3%. (f) Destructive test: stress vs. strain and resistance variation until complete sensor failure at ε = 18.6%. (g) Wearable sensor for radial pulse measurement. (h) Radial pulse signal produced with the strain sensor (sensor driven at 1 μA).

$$SE_R = \quad 10\log_{10}\left(\frac{\sigma}{16\omega\mu_r\varepsilon_0}\right) = 39.5 + 10\log_{10}\left(\frac{\sigma}{2\pi f\mu}\right) \tag{7}$$

where ω, μ_r, ε_0, and f, μ are the angular frequency, relative permeability, vacuum permittivity, frequency, and absolute permeability, respectively. The nonreflected waves go through the surface of the shielding material and are then partially absorbed by dielectric, magnetic, and conduction losses and finally dissipated as heat. For a nonmagnetic and conducting material, the absorption loss (SE_A) can be expressed as [106,107]:

$$SE_A = 8.686 \quad \left(\frac{t}{\delta}\right) = 8.686\sqrt{\pi f\mu\sigma} \tag{8}$$

where t is the sample thickness and δ is the skin depth, which are proportional to the square root of the resistivity. According to our data, a fourfold increase in coating thickness (from 11.6 to 47.8 μm) resulted in a corresponding increase in the SER (from 2.1 to 8.3 dB) but a less significant increase in the SEA (only by a factor of 2.4, from 6.0 to 14.4 dB). As inferred from Eq. 7, the reflection loss (SER) correlates with the impedance mismatch between the coating surface and free space (defined as 377 Ω). Conversely, Eq. 8 explains that absorption (SEA) is primarily determined by the 'skin effect', which refers to the fact that electromagnetic wave absorption in conductive materials occurs primarily at the surface layer. Any waves penetrating beyond this 'skin depth' are significantly weaker, meaning that a further increase in coating thickness beyond this point does not substantially enhance absorption. Therefore, thicker coatings with higher conductivities can i) increase the impedance mismatch, leading to greater reflection loss, and ii) decrease the skin depth, meaning that the majority of the radiation will be absorbed at the surface. The plots in Fig. 8d show the two components contributing to the total SE for sample D (~48 μm). This 50-μm-thick coating can block 99.46% of incoming radiation and achieve a total SE higher than the recommended requirement for commercial applications (20 dB). This performance could be further improved by post processing the coating via compression or thermal treatment to increase the conductivity, as previously reported. For example, graphene laminates (~8 μm thick and with 4.3×10^4 S/m conductivity) compressed on paper reached an SE of 32 dB (12–18 GHz range) [108], while graphene films (3–8 μm thick and ~20 Ω/sq) improved from 20 to 30 dB (1–18 GHz range) [68] after thermal annealing.

3.3. Textile strain sensors

A textile strain sensor was fabricated with the composite paste as described in Experimental Section 2.5 (Fig. 9a) [109–113]. The strain sensor was characterized for increasing tension and then returned to the initial configuration to determine the tensile modulus (E), assess hysteresis in the mechanical and electrical responses, and measure the gauge factor (GF). The assembly of the sensor on a universal testing machine is shown in Fig. 9b. A stress—strain cycle (for $0\% < \varepsilon < 5\%$) is depicted in Fig. 9c), where a linear fit was performed to the loading portion of the curve to extract the tensile modulus ($E = 201.03 \pm 0.10$ kPa). Despite the low linear speed used in the test (0.6 mm/min), considerable hysteresis is observed. The mechanical hysteresis of the sensor (H_M) can be calculated from the stress—strain curve:

$$H_M(\%) = \frac{\left|\sigma_{\varepsilon,up} - \sigma_{\varepsilon,down}\right|_{max}}{\sigma_{max} - \sigma_{min}} \times 100 \tag{9}$$

where $\left|\sigma_{\varepsilon,up} - \sigma_{\varepsilon,down}\right|_{\max}$ is the maximum difference in stress between the loading and unloading parts of the cycle at the same strain ε and σ_{max} and σ_{min} are the maximum and minimum stress values, respectively. At $\varepsilon = 2.65\%$, $\left|\sigma_{\varepsilon,up} - \sigma_{\varepsilon,down}\right|_{\max} = 3174$ Pa. Considering the extreme values $\sigma_{max} = 10944$ Pa and $\sigma_{min} = 184$ Pa, the mechanical hysteresis peaks at $H_M = 29.5\%$. The variation in the electrical resistance of the sensor was measured as a function of the strain (Fig. 9d) to assess the gauge factor, which is defined as

$$GF = \frac{\Delta R/R_0}{\Delta L/L_0} = \frac{\Delta R/R_0}{\varepsilon} \tag{10}$$

where ΔR is the resistance variation relative to the initial resistance (R_0) and ΔL is the length variation relative to the initial gauge length (L_0). The GF is low for $\varepsilon < 0.5\%$, possibly due to considerable overlap and sliding of the conductive nanocarbons within the sensing element. Nevertheless, as the strain increases, the contact resistance starts changing, resulting in an approximately constant $GF = 134 \pm 10$ for $0.5\% < \varepsilon < 4\%$. The obtained GF is comparable to that of previously reported graphene strain sensors [109,112] and MXene-based strain sensors [89] but lower than that of graphene woven fabrics [111]. The GF of the material depends on several parameters and could be increased in the future by various approaches (*e.g.*, thermal postprocessing, micro/nanostructuring, surface engineering, functional doping, etc.) [114]. The electrical hysteresis (H_R) of the sensor can be determined from the measured resistance variations [110]:

$$H_R(\%) = \frac{\left|R_{\varepsilon,up} - R_{\varepsilon,down}\right|_{max}}{R_{max} - R_{min}} \times 100 \tag{11}$$

where $\left|R_{\varepsilon,up} - R_{\varepsilon,down}\right|_{\max}$ is the maximum difference in the resistance between the upward and the downward parts of the loading cycle (at the same strain level ε). R_{max} and R_{min} are the maximum and minimum electrical resistances measured along the complete hysteresis loop, respectively. At $\varepsilon = 3.47\%$ and $\left|R_{\varepsilon,up} - R_{\varepsilon,down}\right|_{\max} = 22.38$ MΩ and considering $R_{max} = 73.15$ MΩ and $R_{min} = 11.92$ MΩ, the electrical hysteresis is $H_R = 36.6\%$, which is only marginally greater than the mechanical hysteresis due to the textile substrate. Therefore, the resistance change exhibits a hysteretic behavior on the same order of magnitude as the mechanical response. This proves that the nanocarbon sensor transduces the mechanical state of the textile substrate with high fidelity since the mechanical hysteresis is connected to the textile property, while the resistance changes are entirely due to the conductive element. The sensitivity of the strain sensor is high because of the high signal-to-noise ratio required to convert mechanical stimuli into a measurable and clear electrical signal. Furthermore, including a stretchable binder in graphene ink will further improve the stretchability of the sensor, thus allowing easy deployment in real-world environments [115]. The sensor repeatability was tested by performing 1000 strain cycles at a peak strain of 3%, corresponding to a 0.36 mm extension of the textile (Fig. 9e). The linear actuator speed was set at 0.05 mm/s, resulting in a cycling period of ~16.5 s. The sensor was stable, and no drift was observed at this strain level. The sensor repeatability can be assessed by the readout variability during the cycling of the sensor [110]:

$$\delta_R(\%) = \frac{\Sigma_{Rmax}}{R_{max} - R_{min}} \times 100 \tag{12}$$

where $\Sigma_{R\max}$ is the variation in electrical resistance, measured at maximum strain, for several cycles. Considering the full aging test, the standard deviation of the resistance at $\varepsilon = 3\%$ is $\Sigma_{R\max} = 1.35\times10^6$, $R_{max} = 28.78$ MΩ and $R_{min} = 2.67$ MΩ. Thus, the sensor readout repeatability is quite low, $\delta_R \sim 5.2\%$, as desired. One of the sensors was tested until failure for increasing strain levels, as shown in Fig. 9f. At $\varepsilon = 8\%$, a sudden increase in resistance is observed, likely due to the first cracks developing in the sensor. With increasing strain, sudden resistance increases are observed due to further cracking of the sensing element until the sensor becomes an open circuit at $\varepsilon \sim 18.6\%$. The textile substrate exhibited nonlinear stress—strain behavior, at least up to $\varepsilon = 50\%$, without failure. Finally, we assembled an easy wearable sensor configuration to realize real pulse measurements on a wrist (Fig. 9g). The sensor was driven by a current source, while an oscilloscope monitored the output voltage over time. A typical signal is

depicted in Fig. 9h, where the heart rate is measured as 71 ± 5 beats per minute (bpm). Other applications of this textile-integrated strain sensor might include monitoring other parameters related to physical activity (such as the breathing rate) or medical devices for patient monitoring [74–76].

4. Conclusions

In this work, we produced stable dispersions of few-layer graphene flakes in water by high-shear mixing and high-pressure airless spray exfoliation, reaching a production rate of 1 L/h (at a 1.4 mg/mL concentration). Our approach is sustainable and inexpensive and thus potentially applicable to high-throughput industrial manufacturing. Graphene flakes were used as primary materials in the development of a nanocarbon-based, viscous, composite paste with high electrical conductivity. The paste was designed to strongly adhere to plastic and flexible substrates when deposited by solution processing techniques, such as bar coating. Proof-of-concept microsupercapacitors fabricated with graphene paste attained a Coulombic efficiency close to 100%, an areal capacitance of 6.16 mF cm^{-2}, a volumetric capacitance of 2.46 F cm^{-3}, and a maximum energy density of 209 μWh cm^{-3}. The devices also showed an excellent capacitance retention of 91.5% after 10000 GCD cycles. When subjected to bending tests, the microsupercapacitors retained their unaltered performance due to the high percolation and mechanical flexibility of the graphene composite paste, which remains easily accessible to the electrolyte. The microsupercapacitors were also assembled in series and parallel configurations to demonstrate their adjustable voltage and capacitance outputs. Electromagnetic interference shielding coatings and textile strain sensors were also fabricated to further prove the multipurpose nature of the composite paste. Coatings with <50 μm thickness reached a shielding effectiveness of ~ 23 dB. The textile strain sensor exhibited a high gauge factor and reliability. Overall, our results provide a pathway for minimizing the environmental impact associated with the production of widespread technologies such as microsupercapacitors, which often require harmful chemicals and contain nonbiodegradable components.

CRediT authorship contribution statement

Andrea Capasso: Writing – review & editing, Validation, Supervision, Resources, Methodology, Funding acquisition, Conceptualization. **Giovanni De Bellis:** Writing – review & editing, Investigation, Formal analysis. **Pedro Alpuim:** Writing – review & editing, Validation, Resources. **Rui S. Sampaio:** Writing – review & editing, Investigation, Formal analysis, Data curation. **Maria Fatima Montemor:** Writing – review & editing, Validation, Resources, Methodology. **Vicente Lopes:** Writing – review & editing, Investigation, Formal analysis, Data curation. **Rui M. R. Pinto:** Writing – review & editing, Investigation, Data curation. **K. B. Vinayakumar:** Writing – review & editing, Validation, Supervision, Resources. **Ernesto Placidi:** Writing – review & editing, Investigation, Formal analysis. **Siva Sankar Nemala:** Writing – review & editing, Writing – original draft, Methodology, Investigation, Formal analysis, Conceptualization. **João Fernandes:** Writing – review & editing, Investigation, Formal analysis. **João Rodrigues:** Writing – review & editing, Investigation, Formal analysis, Data curation.

Declaration of Competing Interest

The authors declare that they have no known competing financial interests or personal relationships that could have appeared to influence the work reported in this paper

Data Availability

Data will be made available on request.

Acknowledgments

We acknowledge the financial support of the "GEMIS-Graphene-enhanced Electro Magnetic Interference Shielding" project with Reference No. POCI-01-0247-FEDER-045939, cofunded by COMPETE 2020—Operational Programme for Competitiveness and Internationalization and FCT—Science and Technology Foundation, under the Portugal 2020 Partnership Agreement, through the European Regional Development Fund. FCT also partially supported this research in the framework of the project "2DM4EH" with reference to DRI/India/0664/2020. EP acknowledges support from PNRR MUR project Rome Technopole-Fp1-CUP B83C22002820006. We thank Mr Guilherme Araújo for the assistance with the AFM measurements, and Graphenest for support with the EMI shielding measurements.

References

[1] K.S. Novoselov, A.K. Geim, S.V. Morozov, D. Jiang, Y. Zhang, S.V. Dubonos, I.V. Grigorieva, A.A. Firsov, Electric Field Effect in Atomically Thin Carbon Films, Kluwer, 2004. ⟨www.arXiv.org/quant-ph/⟩.
[2] D.G. Papageorgiou, I.A. Kinloch, R.J. Young, Mechanical properties of graphene and graphene-based nanocomposites, Prog. Mater. Sci. 90 (2017) 75–127, https://doi.org/10.1016/J.PMATSCI.2017.07.004.
[3] A.K. Geim, K.S. Novoselov, The rise of graphene, Nat. Mater. 6 (2007) 183–191, https://doi.org/10.1038/nmat1849.
[4] K.S. Novoselov, V.I. Fal'Ko, L. Colombo, P.R. Gellert, M.G. Schwab, K. Kim, A roadmap for graphene, Nature 490 (2012) 192–200, https://doi.org/10.1038/nature11458.
[5] D.R. Cooper, B. D'Anjou, N. Ghattamaneni, B. Harack, M. Hilke, A. Horth, N. Majlis, M. Massicotte, L. Vandsburger, E. Whiteway, V. Yu, Experimental review of graphene, ISRN Condens. Matter Phys. 2012 (2012) 1–56, https://doi.org/10.5402/2012/501686.
[6] J. Santos, M. Moschetta, J. Rodrigues, P. Alpuim, A. Capasso, Interactions between 2D materials and living matter: a review on graphene and hexagonal boron nitride coatings, Front Bioeng. Biotechnol. 9 (2021), https://doi.org/10.3389/fbioe.2021.612669.
[7] S.J. Kim, K. Choi, B. Lee, Y. Kim, B.H. Hong, Materials for flexible, stretchable electronics: graphene and 2D materials, Annu Rev. Mater. Res 45 (2015) 63–84, https://doi.org/10.1146/annurev-matsci-070214-020901.
[8] T.H. Han, H. Kim, S.J. Kwon, T.W. Lee, Graphene-based flexible electronic devices, Mater. Sci. Eng. R: Rep. 118 (2017) 1–43, https://doi.org/10.1016/j.mser.2017.05.001.
[9] D. Shahdeo, A. Roberts, N. Abbineni, S. Gandhi, Chapter Eight - Graphene based sensors, in: C.M. Hussain (Ed.), Comprehensive Analytical Chemistry, Elsevier, 2020, pp. 175–199, https://doi.org/10.1016/bs.coac.2020.08.007.
[10] S.W. Bokhari, A.H. Siddique, P.C. Sherrell, X. Yue, K.M. Karumbaiah, S. Wei, A. V. Ellis, W. Gao, Advances in graphene-based supercapacitor electrodes, Energy Rep. 6 (2020) 2768–2784, https://doi.org/10.1016/j.egyr.2020.10.001.
[11] A. Borenstein, O. Hanna, R. Attias, S. Luski, T. Brousse, D. Aurbach, Carbon-based composite materials for supercapacitor electrodes: a review, J. Mater. Chem. A 5 (2017) 12653–12672, https://doi.org/10.1039/C7TA00863E.
[12] A. Velasco, Y.K. Ryu, A. Boscá, A. Ladrón-de-Guevara, E. Hunt, J. Zuo, J. Pedrós, F. Calle, J. Martinez, Recent trends in graphene supercapacitors: from large area to microsupercapacitors, Sustain. Energy Fuels 5 (2021) 1235–1254, https://doi.org/10.1039/D0SE01849J.
[13] J.-H. Ahn, B.H. Hong, Graphene for displays that bend, Nat. Nanotechnol. 9 (2014) 737–738, https://doi.org/10.1038/nnano.2014.226.
[14] E. Fernandes, P.D. Cabral, R. Campos, G. Machado, M.F. Cerqueira, C. Sousa, P. P. Freitas, J. Borme, D.Y. Petrovykh, P. Alpuim, Functionalization of single-layer graphene for immunoassays, Appl. Surf. Sci. 480 (2019) 709–716, https://doi.org/10.1016/j.apsusc.2019.03.004.
[15] S. Nemala, S. Prathapani, P. Kartikay, P. Bhargava, S. Mallick, S. Bohm, Water-based high shear exfoliated graphene-based semi-transparent stable dye-sensitized solar cells for solar power window application, IEEE J. Photo 8 (2018) 1252–1258, https://doi.org/10.1109/JPHOTOV.2018.2858924.
[16] A. Capasso, S. Bellani, A.L. Palma, L. Najafi, A.E. Del Rio Castillo, N. Curreli, L. Cinà, V. Miseikis, C. Coletti, G. Calogero, V. Pellegrini, A. Di Carlo, F. Bonaccorso, CVD-graphene/graphene flakes dual-films as advanced DSSC counter electrodes, 2d Mater. 6 (2019) 035007, https://doi.org/10.1088/2053-1583/ab117e.
[17] A. Capasso, L. Salamandra, G. Faggio, T. Dikonimos, F. Buonocore, V. Morandi, L. Ortolani, N. Lisi, Chemical vapor deposited graphene-based derivative as high-performance hole transport material for organic photovoltaics, ACS Appl. Mater. Interfaces 8 (2016), https://doi.org/10.1021/acsami.6b06749.
[18] X.Y. Wang, A. Narita, K. Müllen, Precision synthesis versus bulk-scale fabrication of graphenes, Nat. Rev. Chem. 2 (2018), https://doi.org/10.1038/S41570-017-0100.
[19] L. Li, M. Zhou, L. Jin, L. Liu, Y. Mo, X. Li, Z. Mo, Z. Liu, S. You, H. Zhu, Research progress of the liquid-phase exfoliation and stable dispersion mechanism and method of graphene, Front Mater. 6 (2019), https://doi.org/10.3389/fmats.2019.00325.

[20] S. Lund, J. Kauppila, S. Sirkiä, J. Palosaari, O. Eklund, R.-M. Latonen, J.-H. Smått, J. Peltonen, T. Lindfors, Fast high-shear exfoliation of natural flake graphite with temperature control and high yield, Carbon N. Y 174 (2021) 123–131, https://doi.org/10.1016/j.carbon.2020.11.094.

[21] W. Zhao, M. Fang, F. Wu, H. Wu, L. Wang, G. Chen, Preparation of graphene by exfoliation of graphite using wet ball milling, J. Mater. Chem. 20 (2010) 5817–5819, https://doi.org/10.1039/C0JM01354D.

[22] P.G. Karagiannidis, S.A. Hodge, L. Lombardi, F. Tomarchio, N. Decorde, S. Milana, I. Goykhman, Y. Su, S.V. Mesite, D.N. Johnstone, R.K. Leary, P. A. Midgley, N.M. Pugno, F. Torrisi, A.C. Ferrari, Microfluidization of graphite and formulation of graphene-based conductive inks, ACS Nano 11 (2017) 2742–2755, https://doi.org/10.1021/acsnano.6b07735.

[23] J. Shang, F. Xue, E. Ding, The facile fabrication of few-layer graphene and graphite nanosheets by high pressure homogenization, Chem. Commun. 51 (2015) 15811–15814, https://doi.org/10.1039/C5CC06151B.

[24] S. Bellani, E. Petroni, A.E. Del Rio Castillo, N. Curreli, B. Martín-García, R. Oropesa-Nuñez, M. Prato, F. Bonaccorso, Scalable production of graphene inks via wet-jet milling exfoliation for screen-printed micro-supercapacitors, Adv. Funct. Mater. 29 (2019) 1807659, https://doi.org/10.1002/adfm.201807659.

[25] U. Khan, H. Porwal, A. O'Neill, K. Nawaz, P. May, J.N. Coleman, Solvent-exfoliated graphene at extremely high concentration, Langmuir 27 (2011) 9077–9082, https://doi.org/10.1021/la201797h.

[26] E. Varrla, K.R. Paton, C. Backes, A. Harvey, R.J. Smith, J. McCauley, J. N. Coleman, Turbulence-assisted shear exfoliation of graphene using household detergent and a kitchen blender, Nanoscale 6 (2014) 11810–11819, https://doi.org/10.1039/C4NR03560G.

[27] G. Hu, J. Kang, L.W.T. Ng, X. Zhu, R.C.T. Howe, C.G. Jones, M.C. Hersam, T. Hasan, Functional inks and printing of two-dimensional materials, Chem. Soc. Rev. 47 (2018) 3265–3300, https://doi.org/10.1039/C8CS00084K.

[28] J.R. Camargo, L.O. Orzari, D.A.G. Araújo, P.R. de Oliveira, C. Kalinke, D.P. Rocha, A. Luiz dos Santos, R.M. Takeuchi, R.A.A. Munoz, J.A. Bonacin, B.C. Janegitz, Development of conductive inks for electrochemical sensors and biosensors, Microchem. J. 164 (2021) 105998, https://doi.org/10.1016/J.MICROC.2021.105998.

[29] W. Yang, C. Wang, Graphene and the related conductive inks for flexible electronics, J. Mater. Chem. C. 4 (2016) 7193–7207, https://doi.org/10.1039/C6TC01625A.

[30] K.R. Paton, E. Varrla, C. Backes, R.J. Smith, U. Khan, A. O'Neill, C. Boland, M. Lotya, O.M. Istrate, P. King, T. Higgins, S. Barwich, P. May, P. Puczkarski, I. Ahmed, M. Moebius, H. Pettersson, E. Long, J. Coelho, S.E. O'Brien, E. K. McGuire, B.M. Sanchez, G.S. Duesberg, N. McEvoy, T.J. Pennycook, C. Downing, A. Crossley, V. Nicolosi, J.N. Coleman, Scalable production of large quantities of defect-free few-layer graphene by shear exfoliation in liquids, Nat. Mater. 13 (2014) 624–630, https://doi.org/10.1038/nmat3944.

[31] L. Liu, Z. Shen, M. Yi, X. Zhang, S. Ma, A green, rapid and size-controlled production of high-quality graphene sheets by hydrodynamic forces, RSC Adv. 4 (2014) 36464–36470, https://doi.org/10.1039/C4RA05635C.

[32] T.S. Tran, N.K. Dutta, N.R. Choudhury, Graphene inks for printed flexible electronics: Graphene dispersions, ink formulations, printing techniques and applications, Adv. Colloid Interface Sci. 261 (2018) 41–61, https://doi.org/10.1016/j.cis.2018.09.003.

[33] A.V. Tyurnina, J.A. Morton, A. Kaur, J. Mi, N. Grobert, K. Porfyrakis, I. Tzanakis, D.G. Eskin, Effects of green solvents and surfactants on the characteristics of few-layer graphene produced by dual-frequency ultrasonic liquid phase exfoliation technique, Carbon N. Y 206 (2023) 7–15, https://doi.org/10.1016/J.CARBON.2023.01.062.

[34] A. Capasso, A.E. Del Rio Castillo, H. Sun, A. Ansaldo, V. Pellegrini, F. Bonaccorso, Ink-jet printing of graphene for flexible electronics: an environmentally-friendly approach, Solid State Commun. 224 (2015) 53–63, https://doi.org/10.1016/j.ssc.2015.08.011.

[35] J. Fernandes, S.S. Nemala, G. De Bellis, A. Capasso, Green Solvents for the Liquid Phase Exfoliation Production of Graphene: The Promising Case of Cyrene, Front Chem. 10 (2022), https://doi.org/10.3389/fchem.2022.878799.

[36] D.H. Gharib, S. Gietman, F. Malherbe, S.E. Moulton, High yield, solid exfoliation and liquid dispersion of graphite driven by a donor-acceptor interaction, Carbon N. Y 123 (2017) 695–707, https://doi.org/10.1016/J.CARBON.2017.08.025.

[37] S. Tkachev, M. Monteiro, J. Santos, E. Placidi, M.Ben Hassine, P. Marques, P. Ferreira, P. Alpuim, A. Capasso, Environmentally friendly graphene inks for touch screen sensors, Adv. Funct. Mater. 31 (2021) 2103287, https://doi.org/10.1002/adfm.202103287.

[38] A. Capasso, A.E. Del Rio Castillo, H. Sun, A. Ansaldo, V. Pellegrini, F. Bonaccorso, Ink-jet printing of graphene for flexible electronics: an environmentally-friendly approach, Solid State Commun. 224 (2015) 53–63, https://doi.org/10.1016/j.ssc.2015.08.011.

[39] D. Linke, Chapter 34 Detergents, Overv., Methods Enzym. 463 (2009) 603–617, https://doi.org/10.1016/S0076-6879(09)63034-2.

[40] J.C.C. Ramirez, T.P. Tumolva, Analysis and optimization of water-based printing ink formulations for polyethylene films, Appl. Adhes. Sci. 6 (1) (2018), https://doi.org/10.1186/s40563-017-0102-z.

[41] H. Sun, A.E. Del Rio Castillo, S. Monaco, A. Capasso, A. Ansaldo, M. Prato, D. A. Dinh, V. Pellegrini, B. Scrosati, L. Manna, F. Bonaccorso, Binder-free graphene as an advanced anode for lithium batteries, J. Mater. Chem. A Mater. 4 (2016) 6886–6895, https://doi.org/10.1039/C5TA08553E.

[42] Z. Salele Iro, A brief review on electrode materials for supercapacitor, Int J. Electrochem Sci. 11 (2016) 10628–10643, https://doi.org/10.20964/2016.12.50.

[43] Q. Ke, J. Wang, Graphene-based materials for supercapacitor electrodes – A review, J. Mater. 2 (2016) 37–54, https://doi.org/10.1016/j.jmat.2016.01.001.

[44] A. Burke, Ultracapacitors: why, how, and where is the technology, J. Power Sources 91 (2000) 37–50, https://doi.org/10.1016/S0378-7753(00)00485-7.

[45] A. González, E. Goikolea, J.A. Barrena, R. Mysyk, Review on supercapacitors: technologies and materials, Renew. Sustain. Energy Rev. 58 (2016) 1189–1206, https://doi.org/10.1016/j.rser.2015.12.249.

[46] L.L. Zhang, X.S. Zhao, Carbon-based materials as supercapacitor electrodes, Chem. Soc. Rev. 38 (2009) 2520–2531, https://doi.org/10.1039/B813846J.

[47] J. Miller, P. Simon, Materials science—electrochemical capacitors for energy management, Science 321 (2008) 651–652, https://doi.org/10.1126/science.1158736.

[48] P. Simon, Y. Gogotsi, Materials for electrochemical capacitors, Nat. Mater. 7 (2008) 845–854, https://doi.org/10.1038/nmat2297.

[49] K. Subasinghage, K. Gunawardane, N. Padmawansa, N. Kularatna, M. Moradian, Modern supercapacitors technologies and their applicability in mature electrical engineering applications, Energy 15 (2022), https://doi.org/10.3390/en15207752.

[50] J. Partridge, D.I. Abouelamaimen, The role of supercapacitors in regenerative braking systems, Energy 12 (2019), https://doi.org/10.3390/en12142683.

[51] X. Chen, N.S. Villa, Y. Zhuang, L. Chen, T. Wang, Z. Li, T. Kong, Stretchable supercapacitors as emergent energy storage units for health monitoring bioelectronics, Adv. Energy Mater. 10 (2020) 1902769, https://doi.org/10.1002/aenm.201902769.

[52] M. Beidaghi, Y. Gogotsi, Capacitive energy storage in micro-scale devices: recent advances in design and fabrication of micro-supercapacitors, Energy Environ. Sci. 7 (2014) 867–884, https://doi.org/10.1039/C3EE43526A.

[53] Z.-S. Wu, X. Feng, H.-M. Cheng, Recent advances in graphene-based planar micro-supercapacitors for on-chip energy storage, Natl. Sci. Rev. 1 (2014) 277–292, https://doi.org/10.1093/nsr/nwt003.

[54] D. Qi, Y. Liu, Z. Liu, L. Zhang, X. Chen, Design of architectures and materials in in-plane micro-supercapacitors: current status and future challenges, Adv. Mater. 29 (2017) 1602802, https://doi.org/10.1002/adma.201602802.

[55] A. Tyagi, K.M. Tripathi, R.K. Gupta, Recent progress in micro-scale energy storage devices and future aspects, J. Mater. Chem. A Mater. 3 (2015) 22507–22541, https://doi.org/10.1039/C5TA05666G.

[56] J. Bae, M.K. Song, Y.J. Park, J.M. Kim, M. Liu, Z.L. Wang, Fiber supercapacitors made of nanowire-fiber hybrid structures for wearable/flexible energy storage, Angew. Chem. - Int. Ed. 50 (2011) 1683–1687, https://doi.org/10.1002/anie.201006062.

[57] K. Jost, D. Stenger, C.R. Perez, J.K. McDonough, K. Lian, Y. Gogotsi, G. Dion, Knitted and screen printed carbon-fiber supercapacitors for applications in wearable electronics, Energy Environ. Sci. 6 (2013) 2698–2705, https://doi.org/10.1039/C3EE40515J.

[58] Y. Yang, Q. Huang, L. Niu, D. Wang, C. Yan, Y. She, Z. Zheng, Waterproof, Ultrahigh areal-capacitance, wearable supercapacitor fabrics, Adv. Mater. 29 (2017) 1606679, https://doi.org/10.1002/adma.201606679.

[59] J. Yin, W. Zhang, N.A. Alhebshi, N. Salah, H.N. Alshareef, Synthesis strategies of porous carbon for supercapacitor applications, Small Methods 4 (2020) 1900853, https://doi.org/10.1002/smtd.201900853.

[60] R. Lakra, R. Kumar, P.K. Sahoo, D. Thatoi, A. Soam, A mini-review: graphene based composites for supercapacitor application, Inorg. Chem. Commun. 133 (2021) 108929, https://doi.org/10.1016/j.inoche.2021.108929.

[61] A. Velasco, Y.K. Ryu, A. Boscá, A. Ladrón-de-Guevara, E. Hunt, J. Zuo, J. Pedrós, F. Calle, J. Martinez, Recent trends in graphene supercapacitors: from large area to microsupercapacitors, Sustain. Energy Fuels 5 (2021) 1235–1254, https://doi.org/10.1039/D0SE01849J.

[62] J. Li, F. Ye, S. Vaziri, M. Muhammed, M.C. Lemme, M. Östling, Efficient inkjet printing of graphene, Adv. Mater. 25 (2013) 3985–3992, https://doi.org/10.1002/adma.201300361.

[63] W.J. Hyun, E.B. Secor, C.-H. Kim, M.C. Hersam, L.F. Francis, C.D. Frisbie, Scalable, self-aligned printing of flexible graphene micro-supercapacitors, Adv. Energy Mater. 7 (2017) 1700285, https://doi.org/10.1002/aenm.201700285.

[64] M. Lotya, P.J. King, U. Khan, S. De, J.N. Coleman, High-concentration, surfactant-stabilized graphene dispersions, ACS Nano 4 (2010) 3155–3162, https://doi.org/10.1021/nn1005304.

[65] M. Kim, H.M. Hwang, G.H. Park, H. Lee, Graphene-based composite electrodes for electrochemical energy storage devices: recent progress and challenges, FlatChem 6 (2017) 48–76, https://doi.org/10.1016/J.FLATC.2017.08.002.

[66] N. Díez, C. Botas, R. Mysyk, E. Goikolea, T. Rojo, D. Carriazo, Highly packed graphene–CNT films as electrodes for aqueous supercapacitors with high volumetric performance, J. Mater. Chem. A 6 (2018) 3667–3673, https://doi.org/10.1039/C7TA10210K.

[67] G. Wang, X. Sun, F. Lu, H. Sun, M. Yu, W. Jiang, C. Liu, J. Lian, Flexible pillared graphene-paper electrodes for high-performance electrochemical supercapacitors, Small 8 (2012) 452–459.

[68] C. Acquarelli, A. Rinaldi, A. Tamburrano, G. De Bellis, A.G. D'Aloia, M.S. Sarto, Graphene-based EMI shield obtained via spray deposition technique, : 2014 Int. Symp. . Electromagn. Compat. (2014) 488–493, https://doi.org/10.1109/EMCEurope.2014.6930956.

[69] M.-S. Cao, X.-X. Wang, W.-Q. Cao, J. Yuan, Ultrathin graphene: electrical properties and highly efficient electromagnetic interference shielding, J. Mater. Chem. C. 3 (2015) 6589–6599, https://doi.org/10.1039/C5TC01354B.

[70] C. Liang, Z. Gu, Y. Zhang, Z. Ma, H. Qiu, J. Gu, Structural design strategies of polymer matrix composites for electromagnetic interference shielding: a review, Nanomicro Lett. 13 (2021) 181, https://doi.org/10.1007/s40820-021-00707-2.

[71] Y.J. Jeon, J.H. Yun, M.S. Kang, Analysis of electromagnetic shielding properties of a material developed based on silver-coated copper core-shell spraying, Materials 15 (2022), https://doi.org/10.3390/ma15155448.

[72] S.K. Hong, K.Y. Kim, T.Y. Kim, J.H. Kim, S.W. Park, J.H. Kim, B.J. Cho, Electromagnetic interference shielding effectiveness of monolayer graphene, Nanotechnology 23 (2012), https://doi.org/10.1088/0957-4484/23/45/455704.

[73] Z.P. Wu, D.M. Cheng, W.J. Ma, J.W. Hu, Y.H. Yin, Y.Y. Hu, Y.S. Li, J.G. Yang, Q. F. Xu, Electromagnetic interference shielding effectiveness of composite carbon nanotube macro-film at a high frequency range of 40 GHz to 60 GHz, AIP Adv. 5 (2015) 067130, https://doi.org/10.1063/1.4922599.

[74] K. Keum, S.S. Cho, J.W. Jo, S.K. Park, Y.H. Kim, Mechanically robust textile-based strain and pressure multimodal sensors using metal nanowire/polymer conducting fibers, IScience 25 (2022) 104032, https://doi.org/10.1016/J.ISCI.2022.104032.

[75] Y. Wei, X. Li, Y. Wang, T. Hirtz, Z. Guo, Y. Qiao, T. Cui, H. Tian, Y. Yang, T.-L. Ren, Graphene-based multifunctional textile for sensing and actuating, ACS Nano 15 (2021) 17738–17747, https://doi.org/10.1021/acsnano.1c05701.

[76] X. Zhang, L. Ke, X. Zhang, F. Xu, Y. Hu, H. Lin, J. Zhu, Breathable and wearable strain sensors based on synergistic conductive carbon nanotubes/cotton fabrics for multi-directional motion detection, ACS Appl. Mater. Interfaces 14 (2022) 25753–25762, https://doi.org/10.1021/acsami.2c04790.

[77] R.M.R. Pinto, S.S. Nemala, M. Faraji, J. Fernandes, C. Ponte, G. De Bellis, A. Retolaza, K.B. Vinayakumar, A. Capasso, Material jetting of carbon nano onions for printed electronics, Nanotechnology 34 (2023) 365710, https://doi.org/10.1088/1361-6528/acdad7.

[78] H.W. Choi, D.-W. Shin, J. Yang, S. Lee, C. Figueiredo, S. Sinopoli, K. Ullrich, P. Jovančić, A. Marrani, R. Momentè, J. Gomes, R. Branquinho, U. Emanuele, H. Lee, S.Y. Bang, S.-M. Jung, S.D. Han, S. Zhan, W. Harden-Chaters, Y.-H. Suh, X.-B. Fan, T.H. Lee, M. Chowdhury, Y. Choi, S. Nicotera, A. Torchia, F. M. Moncunill, V.G. Candel, N. Durães, K. Chang, S. Cho, C.-H. Kim, M. Lucassen, A. Nejim, D. Jiménez, M. Springer, Y.-W. Lee, S. Cha, J.I. Sohn, R. Igreja, K. Song, P. Barquinha, R. Martins, G.A.J. Amaratunga, L.G. Occhipinti, M. Chhowalla, J. M. Kim, Smart textile lighting/display system with multifunctional fibre devices for large scale smart home and IoT applications, Nat. Commun. 13 (2022) 814, https://doi.org/10.1038/s41467-022-28459-6.

[79] H. Lee, G. Jung, K. Keum, J.W. Kim, H. Jeong, Y.H. Lee, D.S. Kim, J.S. Ha, A Textile-Based Temperature-Tolerant Stretchable Supercapacitor for Wearable Electronics, Adv. Funct. Mater. 31 (2021) 2106491, https://doi.org/10.1002/adfm.202106491.

[80] W. He, C. Wang, H. Wang, M. Jian, W. Lu, X. Liang, X. Zhang, F. Yang, Y. Zhang, Integrated textile sensor patch for real-time and multiplex sweat analysis, Sci. Adv. 5 (2023) eaax0649, https://doi.org/10.1126/sciadv.aax0649.

[81] J. Wang, C. Lu, K. Zhang, Textile-based strain sensor for human motion detection, ENERGY Environ. Mater. 3 (2020) 80–100, https://doi.org/10.1002/eem2.12041.

[82] D. Yao, Z. Tang, L. Zhang, R. Li, Y. Zhang, H. Zeng, D. Du, J. Ouyang, Gas-permeable and highly sensitive, washable and wearable strain sensors based on graphene/carbon nanotubes hybrids e-textile, Compos Part A Appl. Sci. Manuf. 149 (2021) 106556, https://doi.org/10.1016/j.compositesa.2021.106556.

[83] Z. Yang, Y. Pang, X. Han, Y. Yang, J. Ling, M. Jian, Y. Zhang, Y. Yang, T.-L. Ren, Graphene textile strain sensor with negative resistance variation for human motion detection, ACS Nano 12 (2018) 9134–9141, https://doi.org/10.1021/acsnano.8b03391.

[84] Y. Zhou, C. Myant, R. Stewart, Multifunctional and stretchable graphene/textile composite sensor for human motion monitoring, J. Appl. Polym. Sci. 139 (2022) e52755, https://doi.org/10.1002/app.52755.

[85] R. Yu, C. Zhu, J. Wan, Y. Li, X. Hong, Review of graphene-based textile strain sensors, with emphasis on structure activity relationship, Polymers 13 (2021) 1–22, https://doi.org/10.3390/polym13010151.

[86] R. Banavath, S.S. Nemala, S.-H. Kim, S. Bohm, M.Z. Ansari, D. Mohapatra, P. Bhargava, Industrially scalable exfoliated graphene nanoplatelets by high-pressure airless spray technique for high-performance supercapacitors, FlatChem 33 (2022) 100373, https://doi.org/10.1016/j.flatc.2022.100373.

[87] X. Tong. Advanced Materials and Design for Electromagnetic Interference Shielding, 1st ed., CRC Press, 2008.

[88] M. Peng, F. Qin, Clarification of basic concepts for electromagnetic interference shielding effectiveness, J. Appl. Phys. 130 (2021) 225108, https://doi.org/10.1063/5.0075019.

[89] R. Keller, Design for electromagnetic compatibility–in a nutshell: theory and practice, 1st ed, Springer, 2023.

[90] S.S. Nemala, P. Kartikay, K. S. Aneja, P. Bhargava, H.L.M. Bohm, S. Bohm, S. Mallick, Novel high pressure exfoliated graphene-based semitransparent stable dsscs for building integrated photovoltaics, ACS Appl. Energy Mater. 1 (2018) 2512–2519, https://doi.org/10.1021/acsaem.8b00254.

[91] N. Lisi, T. Dikonimos, F. Buonocore, M. Pittori, R. Mazzaro, R. Rizzoli, S. Marras, A. Capasso, Contamination-free graphene by chemical vapor deposition in quartz furnaces, Sci. Rep. 7 (2017), https://doi.org/10.1038/s41598-017-09811-z.

[92] A.C. Ferrari, J.C. Meyer, V. Scardaci, C. Casiraghi, M. Lazzeri, F. Mauri, S. Piscanec, D. Jiang, K.S. Novoselov, S. Roth, A.K. Geim, Raman spectrum of graphene and graphene layers, Phys. Rev. Lett. 97 (2006) 187401, https://doi.org/10.1103/PhysRevLett.97.187401.

[93] A.C. Ferrari, D.M. Basko, Raman spectroscopy as a versatile tool for studying the properties of graphene, Nat. Nanotechnol. 8 (2013) 235, https://doi.org/10.1038/nnano.2013.46.

[94] M.V. Bracamonte, G.I. Lacconi, S.E. Urreta, L.E.F. Foa Torres, On the nature of defects in liquid-phase exfoliated graphene, J. Phys. Chem. C. 118 (2014) 15455–15459, https://doi.org/10.1021/jp501930a.

[95] L.M. Malard, M.A.A. Pimenta, G. Dresselhaus, M.S. Dresselhaus, Raman spectroscopy in graphene, Phys. Rep. 473 (2009) 51–87, https://doi.org/10.1016/j.physrep.2009.02.003.

[96] S.N. Sankar, J. Fernandes, M.B. dos Santos, B. Espiña, P. Alpuim, A.G. Díez, S. Lanceros-Mendez, L. Saini, S. Kaushik, G. Kalon, A. Capasso, Stable graphene membranes for selective ion transport and emerging contaminants removal in water, Adv. Funct. Mater. 33 (2023) 2214889, https://doi.org/10.1002/adfm.202214889.

[97] M. Lotya, Y. Hernandez, P.J. King, R.J. Smith, V. Nicolosi, L.S. Karlsson, F. M. Blighe, S. De, W. Zhiming, I.T. McGovern, G.S. Duesberg, J.N. Coleman, Liquid phase production of graphene by exfoliation of graphite in surfactant/water solutions, J. Am. Chem. Soc. 131 (2009) 3611–3620, https://doi.org/10.1021/ja807449u.

[98] M. Kim, J.H. Jeong, J.-Y. Lee, A. Capasso, F. Bonaccorso, S.-H. Kang, Y.-K. Lee, G.-H. Lee, Electrically conducting and mechanically strong graphene–polylactic acid composites for 3D printing, ACS Appl. Mater. Interfaces 11 (2019) 11841–11848, https://doi.org/10.1021/acsami.9b03241.

[99] S. Belviso, A. Capasso, E. Santoro, L. Najafi, F. Lelj, S. Superchi, D. Casarini, C. Villani, D. Spirito, S. Bellani, A.E. Del Rio-Castillo, F. Bonaccorso, Thioethyl-porphyrazine/nanocarbon hybrids for photoinduced electron transfer, Adv. Funct. Mater. 28 (2018) 1705418, https://doi.org/10.1002/adfm.201705418.

[100] M.I. Ortiz-Torres, M. Fernández-Niño, J.C. Cruz, A. Capasso, F. Matteocci, E. J. Patiño, Y. Hernández, A.F. González Barrios, Rational design of photo-electrochemical hybrid devices based on graphene and chlamydomonas reinhardtii light-harvesting proteins, Sci. Rep. 10 (2020) 3376, https://doi.org/10.1038/s41598-020-60408-5.

[101] S. Ardizzone, G. Fregonara, S. Trasatti, Inner" and "outer" active surface of RuO2 electrodes, Electro Acta 35 (1990) 263–267, https://doi.org/10.1016/0013-4686(90)85068-X.

[102] X. Shi, S. Pei, F. Zhou, W. Ren, H.-M. Cheng, Z.-S. Wu, X. Bao, Ultrahigh-voltage integrated micro-supercapacitors with designable shapes and superior flexibility, Energy Environ. Sci. 12 (2019) 1534–1541, https://doi.org/10.1039/C8EE02924E.

[103] J. Li, S. Sollami Delekta, P. Zhang, S. Yang, M.R. Lohe, X. Zhuang, X. Feng, M. Östling, Scalable fabrication and integration of graphene microsupercapacitors through full inkjet printing, ACS Nano 11 (2017) 8249–8256, https://doi.org/10.1021/acsnano.7b03354.

[104] J. Zhao, Q. Shi, Y. Guo, X. Wang, D. Wang, F. Tan, L. Jiang, Y. Yu, Flash foam stamp-inspired fabrication of flexible in-plane graphene integrated micro-supercapacitors on paper, J. Power Sources 433 (2019) 226703, https://doi.org/10.1016/J.JPOWSOUR.2019.226703.

[105] Z. Yao, B. Quan, T. Yang, J. Li, C. Gu, Flexible supercapacitors based on vertical graphene/carbon fabric with high rate performance, Appl. Surf. Sci. 610 (2023), https://doi.org/10.1016/j.apsusc.2022.155535.

[106] H. Ott. Electromagnetic Compatibility Engineering, 1st ed., Wiley, 2009.

[107] J. Hong, J. Kwon, D. Im, J. Ko, C.Y. Nam, H.G. Yang, S.H. Shin, S.M. Hong, S. S. Hwang, H.G. Yoon, A.S. Lee, Best practices for correlating electrical conductivity with broadband EMI shielding in binary filler-based conducting polymer composites, Chem. Eng. J. 455 (2023) 140528, https://doi.org/10.1016/j.cej.2022.140528.

[108] M. Al-Aqeeli, A. Alburaikan, J. Chen, T. Leng, Z. Hu, K. Chang, X. Huang, Electromagnetic interference shielding based on highly flexible and conductive graphene laminate, Electron Lett. 51 (2015), https://doi.org/10.1049/el.2015.2299.

[109] X. Chen, X. Zheng, J.-K. Kim, X. Li, D.-W. Lee, Investigation of graphene piezoresistors for use as strain gauge sensors, J. Vac. Sci. Technol. B, Nanotechnol. Microelectron.: Mater., Process., Meas., Phenom. 29 (2011) 06FE01, https://doi.org/10.1116/1.3660784.

[110] Q. Li, Y. Wang, S. Jiang, T. Li, X. Ding, X. Tao, Xi Wang, Investigation into tensile hysteresis of polyurethane-containing textile substrates for coated strain sensors, Mater. Des. 188 (2019) 108451, https://doi.org/10.1016/j.matdes.2019.108451.

[111] X. Li, R. Zhang, W. Yu, K. Wang, J. Wei, D. Wu, A. Cao, Z. Li, Y. Cheng, Q. Zheng, R.S. Ruoff, H. Zhu, Stretchable and highly sensitive graphene-on-polymer strain sensors, Sci. Rep. 2 (2012) 870, https://doi.org/10.1038/srep00870.

[112] Z. Li, H. Ning, N. Hu, Y. Li, L. Qiao, Giant piezoresistive gauge factor in vein-membrane/graphene sensors with a wide linear working range, J. Mater. Chem. C. Mater. 8 (2020) 16957–16966, https://doi.org/10.1039/D0TC02930K.

[113] Y. Ma, N. Liu, L. Li, X. Hu, Z. Zou, J. Wang, S. Luo, Y. Gao, A highly flexible and sensitive piezoresistive sensor based on MXene with greatly changed interlayer distances, Nat. Commun. 8 (2017) 1207, https://doi.org/10.1038/s41467-017-01136-9.

[114] H. Chen, F. Zhuo, J. Zhou, Y. Liu, J. Zhang, S. Dong, X. Liu, A. Elmarakbi, H. Duan, Y. Fu, Advances in graphene-based flexible and wearable strain sensors, Chem. Eng. J. 464 (2023) 142576, https://doi.org/10.1016/j.cej.2023.142576.

[115] L. Wang, J. Choi, Highly stretchable strain sensors with improved sensitivity enabled by a hybrid of carbon nanotube and graphene, Micro Nano Syst. Lett. 10 (2022) 17, https://doi.org/10.1186/s40486-022-00160-9.

Siva Sankar Nemala is a material scientist and physicist. He received his PhD from Metallurgical Engineering and Materials Science from Indian Institute of Technology Bombay, India in 2019. His PhD thesis focussed on Graphene synthesis by liquid phase exfoliation methods for photovoltaic applications. Prior to joining INL, he worked as a researcher in the Physics discipline at Indian Institute of Technology Gandhinagar, India. He joined INL in 2021, where he is working on advanced liquid phase exfoliation methods for 2D crystals technology.

João Fernandes earned his integrated MSc degree in Physics Engineering in December 2021. His Master Thesis, titled "Large-scale, controlled growth of two-dimensional materials by Chemical Vapor Deposition," was a collaborative effort with the International Iberian Nanotechnology Laboratory (INL) in Portugal. In early 2022, João joined INL as a junior research fellow, where he extended his expertise in the growth and characterization of 2D materials. Since February 2023, he is a PhD student in the Ameloot group at KU Leuven, Belgium. He is focusing on the development of MOF-based capacitive sensors for the selective detection of volatile organic compounds.

João Rodrigues is currently a research engineer at the International Iberian Nanotechnology Laboratory (Braga, Portugal), with his work dedicated to lithium recovery from recycled batteries. He obtained his Integrated Master's Degree in Micro and Nanotechnology Engineering from FCT-NOVA (Portugal, 2018) and shortly after started working as researcher for the synthesis and characterization of 2D materials via exfoliation and chemical vapor deposition. Additionally, he also has over 3 years of experience as an R&D engineer at Graphenest, focusing his efforts on the development of graphene-based materials and solutions tailored for EMI shielding applications.

Vicente Lopes graduated in Physics Engineering in 2023. He then obtained his MSc in Physics Engineering in 2024, with specialization in devices, microsystems and nanotechnologies. His research focused on integrating glucose sensing platforms into contact lenses using graphene-based technology. Since April 2024, Vicente is a Junior Research Fellow at the International Iberian Nanotechnology Laboratory (Portugal), working on 2D material growth and characterization, as well as nanoelectronic device fabrication.

Rui M. R. Pinto received his PhD degree in biotechnology and biosciences from Instituto Superior Técnico, University of Lisbon, in 2020. His thesis was developed at INESC MN and focused on the development of thin-film silicon MEMS for mass sensing and biosensing applications. He joined INL in 2021, where he optimized inkjet heads and printing processes for the additive manufacturing of flexible electronics using functional inks. Currently, he works on gas sensing for flue gas analysis and environmental monitoring.

K. B. Vinayakumar received the PhD degree from the Indian Institute of Science, Bengaluru, India, in 2016. He was a Post-Doctoral Associate with Cornell University, Ithaca, NY, USA, from 2016 to 2018. Since 2018, he has been with the International Iberian Nanotechnology Laboratory (INL), Braga, Portugal, as a Staff Researcher, with a research focus on multi-gas detection, additive manufacturing, ferroelectret sensors, energy harvesters, micro- and nanofabrication, and flexible wearable devices for healthcare applications.

Ernesto Placidi is Associate Professor of Experimental Matter Physics in the Physics department of Sapienza University of Rome. From 2009–2019 he has been researcher for the Italian National Research Council. He earned a MSc degree and a PhD in Physics in the University of Rome Tor Vergata. His work focuses on growth and study of semiconductor heterostructures, 2D materials and generally materials for energy applications. He has participations and/or responsibility in many national and international projects.

Giovanni De Bellis received both the Laurea degree in Materials Engineering and the PhD degree in Electrical Engineering (scholarship in Nanotechnology), from the University of Rome "Sapienza". Since 2019, he has held the position of Associate Professor of Electrical Engineering at the Department of Astronautical, Electrical and Energy Engineering (DIAEE) of Sapienza University. His research interests cover the development of polymer nanocomposites for EMI shielding applications, radar absorbing materials, strain sensors, sweat and humidity sensors. More recently, his interests have shifted towards soft electrostatic actuators and conductive inks for flexible electrodes.

Pedro Alpuim holds a Ph.D. in Materials Engineering from IST-Lisbon (2003), where he worked on thin-film silicon devices on plastic substrates for flexible electronics. Since then, he has been a professor at the Physics Department of the University of Minho. He is also with the International Iberian Nanotechnology Laboratory (INL), Braga, where he has been a group leader since 2016. His group grows graphene and other 2D materials by CVD and LPE, fabricating bio-sensing devices at the wafer scale, different environmental sensors, and opto-electronic devices. His research interests include single photon emitters from hBN and devices based on light-matter interactions.

Rui S. Sampaio is a post-doctoral researcher at Instituto Superior Técnico, Department of Chemical Engineering. Presently, his scientific activity aims to develop high-performance materials for energy storage. The main fields of interest are energy storage and conversion materials, conducting polymers, electrodeposition, and electrochemical sensors. He is a co-author of 5 scientific papers, with a h index of 3.

Maria F. Montemor is Full Professor at Instituto Superior Técnico, Department of Chemical Engineering. Her scientific activity focuses on new functional coatings for surface protection and for energy storage. She coordinates the Electrochemical Energy Storage research hub and a master program in Energy storage. She is co-author of 20 book chapters and 300 scientific papers, with a h index of 72. She has been awarded with the EFC medal and has received a doctor honoris causa degree by University of Mons. She is co-founder of the company "Charge2C-NewCap" that fabricates supercapacitors.

Andrea Capasso is a permanent Staff Researcher at the International Iberian Nanotechnology Laboratory (INL), where he is principal investigator of scientific and industrial projects focused on the production and application of graphene and 2D materials. He received a MSc in Electronic Engineering from the University of Roma TRE and a PhD in Nanotechnology from the Queensland University of Technology (2012). A former Marie Curie fellow, Andrea held research positions in Australia, Italy, and Korea. His research spans diverse technological areas, including nanoelectronics, energy, neuromorphic engineering, and water treatment.